Acta Neuropathologica Communications https://doi.org/10.1186/s40478-026-02291-1

Article in Press

Timing of microglial ablation determines protection from tau-mediated neurodegeneration and cognitive decline

Received: 6 October 2025

Accepted: 30 March 2026

Published online: 10 April 2026

Cite this article as: Trigo-Alonso P., Luengo E., Fernández-Mendiví C. *et al.* Timing of microglial ablation determines protection from tau-mediated neurodegeneration and cognitive decline. *acta neuropathol commun* (2026). https://doi.org/10.1186/s40478-026-02291-1

Paula Trigo-Alonso, Enrique Luengo, Cristina Fernández-Mendiví, Lucía Viqueira, Nuria García-Magro, Eric Sastre, Juan Antonio Bernal, Pilar Negredo & Manuela G. López

Timing of Microglial Ablation Determines Protection from Tau-Mediated Neurodegeneration and Cognitive Decline

*Paula Trigo-Alonso[1], *Enrique Luengo[1], Cristina Fernández-Mendivíl[1], Lucía Viqueira[1], Nuria García-Magro[4,5], Eric del Sastre[1], Juan Antonio Bernal[3], Pilar Negredo[4] and Manuela G. López[1,2]

[1]Department of Pharmacology. School of Medicine. Universidad Autónoma Madrid. Madrid, Spain

[2]Instituto de Investigación del Hospital de la Princesa. Madrid. Spain

[3]Myocardial Pathophysiology Area, Centro Nacional de Investigaciones Cardiovasculares (CNIC), Madrid, Spain.

[4]Departmento de Anatomía, Histología y Neurociencia. Facultad de Medicina. Universidad Autónoma de Madrid, Madrid, Spain.

[5]Facultad de Ciencias de la Salud, Universidad Francisco de Vitoria, Pozuelo de Alarcón, 28223 Madrid, Spain

**Equal Contributors*

Correspondence to: Dr. Manuela G. Lopez. Department of Pharmacology. School of Medicine. Universidad Autónoma de Madrid. C/ Arzobispo Morcillo 4. Madrid 28029. Spain. E-mail. manuela.garcia@uam.es. Phone +34 914975386

Key words: Tauopathy, microglia, PLX5622, neurodegeneration, cognitive decline

ABSTRACT

Tauopathies comprise a diverse group of neurodegenerative diseases characterized by intracellular aggregation of the microtubule-associated protein tau, neuroinflammation, and neuronal loss. Since tau pathology shows the strongest correlation with cognitive decline in Alzheimer's disease, understanding how microglia contribute to tau-mediated neurodegeneration remains a critical question. Here, we validated a tauopathy mouse model that progressively recapitulates key pathological features of tauopathy. Bilateral hippocampal injection of AAV-hTau^{P301L} (AAV-hTau) resulted in widespread tau accumulation, early and sustained gliosis, complement component 1q (C1q) deposition, progressive reduction of hippocampal layer thickness and cognitive deficits. Notably, we observed marked activation of Cluster of Differentiation 68 (CD68^{+}) microglia and the emergence of Complement 3 (C3^{+}) reactive astrocytes, which developed in parallel over time. To dissect the role of microglia in tau-driven pathology, we depleted them at different stages using the colony-stimulating factor 1 receptor (CSF1R) inhibitor PLX5622. Microglial ablation conferred significant neuroprotection, with early depletion effectively mitigating cognitive decline and structural changes in hippocampal layers supporting an important role for microglial activation in tauopathy progression. Neuroprotection may result from decreased levels of insoluble p-tau oligomers, partial blockade of C3^{+} astrocyte induction and attenuation of microglial reactivity. Overall, our results support the potential of microglia-directed interventions as a promising therapeutic avenue for mitigating disease progression in tauopathies.

BACKGROUND

Tauopathies are a group of neurodegenerative diseases, including Alzheimer's disease (AD), progressive supranuclear palsy (PSP), and corticobasal degeneration (CBD), among others. These disorders are characterized by the accumulation of intracellular tau aggregates; a process associated with dysregulated post-translational modifications (PTMs) of the tau protein. A defining feature of these disorders is the accumulation of fibrillary tangles in the brain, composed of misfolded, hyperphosphorylated tau. While the mechanisms driving tau aggregation remain incompletely understood, growing evidence suggests that neuroinflammation exacerbates tau pathology and contributes to disease progression [1,2]. Furthermore, tau aggregation itself may exacerbate inflammation through feed-forward mechanisms, intensifying the initial neurotoxic damage [3].

Microglial cells are the resident myeloid cells of the CNS, they act as resident phagocytes responding to changes in the environment and play crucial roles in CNS tissue maintenance, injury response, and pathogen defence [4,5]. Over the past 20 years, genome-wide association studies (GWAS) have identified several AD risk variants in genes predominantly expressed in microglia (e.g. APOE, TREM2, CD33, CR1) [6,7]. Also, GWAS studies have identified innate immune pathways that implicate microglia in human tauopathy [8]. Related to tauopathy, microglia can secrete toxic factors to directly [5] or indirectly, through activation of astrocytes, injure neurons [9]; exacerbate tau pathology [2] and its spreading [10]; promote direct synapse loss via microglial phagocytosis or via activation of the complement cascade [11–13]. Although all these events have been recognized in tauopathy, how they evolve with disease progression, and which is the limiting role of microglia in these pathological pathways is still poorly understood.

Microglial survival and proliferation are critically dependent on CSF1R signalling

pathway [14]. In this context, CSF1R inhibitors like PLX5622 can achieve microglial depletion with high efficiency [15]. To understand the role of microglia in tauopathy progression and cognitive impairment we have first characterized the timeline of events occurring in a humanized tauopathy model by intrahippocampal injection of AAV expressing the human tau protein with the P301L mutation in mice. Thereafter, we have induced microglial depletion with PLX5622 at different check points of tauopathy progression to identify which are the limiting processes related to microglia and to determine if microglial depletion can be of therapeutic relevance. We have found that depletion of microglia before overt neurodegeneration confers neuroprotection and prevents cognitive decline, in association with reduced p-tau accumulation, attenuated microgliosis, decreased C1q deposition and partial suppression of reactive astrocytes. Collectively, these findings provide evidence that microglial activation is a major driver for structural alterations in hippocampal layers and cognitive decline in tauopathy and supports microglia-targeted therapies as a promising approach to slowing tau-driven neurodegeneration.

MATERIALS AND METHODS

Animal usage and care

C57BL/6 wild-type (WT) mice were purchased from Charles River and bred in-house. Three-to-five-months-old male mice (25–30 g) were used. They were maintained in a conventional animal facility at Autonomous University of Madrid, Spain, on a 12 h light/12 h dark cycle, with food and water *ad libitum*. All procedures involving animals were performed following the Guide for Care and Use of Laboratory Animals and approved by the Institutional Ethics Committee of Autonomous University of Madrid and the Comunidad Autónoma of Madrid, Spain, (PROEX 252/16 and PROEX 218.5/20) following the European Guidelines for the use and care of animals for research in accordance with the European Union Directive of

September 22, 2010 (2010/63/UE) and with the Spanish Royal Decree of February 1, 2013 (53/2013). All efforts were made to minimize animal suffering and to reduce the number of animals used.

Adeno-associated viral vectors

Adeno-associated viral (AAV) vectors 2/6- synapsin-1 (SYN1)-EGFP (AAV-GFP) and AAV2/6-SYN1-humanTauP301L (AAV-AAV-hTau) were produced and purified as previously described [16]. Briefly, AAV vectors were all produced by the double transfection method using HEK 293A cells. AAV plasmids were cloned and propagated in the Stbl3 *Escherichia coli* strain (Life Technologies). Shuttle plasmid pAAV-hTauP301L and pAAV-GFP were described previously [17] and packaged into capsids from AAV-6, using helper plasmid pDP6rs (providing the three adenoviral helper genes, rep and cap AAV viral genes), obtained from Plasmid Factory. The AAV shuttle and helper plasmids were transfected into HEK 293A cells by calcium phosphate co-precipitation. A total of 840 µg plasmid DNA (mixed in an equimolar ratio) were used per HYPERFlask (Corning) seeded with 1.2 × 108 cells the day before. Seventy-two hours after transfection, the cells were collected by centrifugation and the cell pellet was resuspended in TMS (50 mmol/L Tris-HCl, 150 mmol/L NaCl, 2 mmol/L Na2Mg) on ice before digestion with DNase I and RNaseA (0.1 mg/mL each; Roche) at 37°C for 60 minutes. Clarified supernatant containing the viral particles was obtained by iodixanol gradient centrifugation (10800712). Gradient fractions containing virus were concentrated using Amicon UltraCel columns (Millipore) and stored at −70°C.

Induction of tauopathy *in vivo*

Mice were anesthetized with Isoflutek (Isofluorane 1000 mg/g) in oxygen under spontaneous respiration (induction at 5 % and maintenance at 2 %). Subsequently, mice

were placed in a stereotaxic instrument (Stoeling) and their temperature was monitored with a controlled rectal probe heating pad (Cibertec). Tauopathy was induced by bilateral intrahippocampal (IHP) delivery of AAV-hTau^{P301L,} and control mice were AAV-GFP-injected. After an incision in the cranial midline, the skull was perforated with a micro drill at 1.94 mm posterior and 1.4 medio lateral to bregma on the left and right side. Then, using an automatic Hamilton syringe (1701 RN Neuros Syringe), 1.01 µL of AVVs ($4.34x10^{12}$ VP/ml) were injected bilaterally 1.8 mm below the dura mater (0.15 µL/min). After surgery, mice were housed for postoperative monitoring and kept until the end of the experiment. At final time point, mice were anesthetized with 5 % isoflurane and sacrificed by decapitation for western blotting or intracardiacally perfused through the ascending aorta with 0.9% NaCl, followed by 4% PFA in 0.1 M phosphate buffer (PB, pH 7.4) for immunofluorescence studies.

Microglial depletion protocols

PLX5622 was provided by Plexxikon Inc. and formulated in AIN-76A standard chow by Research Diets Inc. at 1200 ppm. To eliminate microglia, PLX5622 was administered during the time points indicated in the results section. Control animals received the same AIN-76A diet formulation without PLX5622, ensuring that all dietary components were identical between groups and that the only experimental variable was CSF1R inhibition.

Isolation of insoluble and soluble fractions of hippocampal tissue

The protocol previously described by [18] with some modifications was used. The hippocampal tissue from the left hemisphere was homogenized in Buffer A (0.1 M MES Buffer pH7.0, 1 M sucrose, 0.5 mM $MgSO_4$, 1 mM EDTA, 1 mM NaF, 1 mM Na_3VO_4, 10 µg/ml leupeptine and phenylmethylsulfonyl fluoride (PMSF) and centrifuged at 20.000 rpm for 20 minutes at 4 °C. To obtain the SI fractions, pellets were resuspended in RAB buffer

1 % sarkosyl (0.1M MES Buffer pH6.8, 10% sucrose, 0.5 mM MgSO4, 2mM EGTA, 0.5 M NaCl, 1 mM $MgCl_2$, 10 mM Na_2HPO4, 20mM NaF, 1 mM Na_3VO_4, 10 µg/ml leupeptine and PMSF, and 1% sarkosyl). Then, samples were vortexed for 1 minute at room temperature (RT), rotated at 4 °C overnight and centrifuged at 69.000 rpm for 30 minutes at 4 °C. SS fractions were collected from the supernatants and SI fractions were obtained by resuspending the pellets in RAB buffer 1% sarkosyl.

Western blotting

Hippocampal tissue was lysed in 150 µL of ice-cold Lysis Buffer (137 mM NaCl, 20 mM NaF, 10 % glycerol, 20 mM Tris—HCl, 1 % Nonidet P–40, 1µg/mL leupeptin, 1mM PMSF, 1 mM sodium pyrophosphate, and 1 mM Na_3VO_4, pH 7.5). 20 µg of SS, SI or protein extracts were resolved in SDS–PAGE transferred to Immobilon–P PVDF membranes (Millipore). Ponceau (Cephan Life Sciences) staining was used as loading control. Membranes were activated with methanol and blocked with 4 % bovine serum albumin (BSA) in Tris–buffered saline –Tween (TTBS) (10 mM Tris, 150 mM NaCl; 0.2 % Tween–20, pH 7.4) for 2 hours and then incubated with the primary antibody **(Table 1).** Then, washed thrice with TTBS and incubated with the appropriate peroxidase-conjugated secondary antibody (1:10,000; Santa Cruz Biotechnology) for 45 minutes. Thereafter, membranes were washed thrice with TTBS, incubated with ECL-Advance Western-blotting Detection Kit (GE Healthcare), exposed using a ChemicDoC MP System (Bio-Rad Laboratories) and specific immunoreactive bands were quantified using Fiji software.

Immunofluorescence

Brains were post-fixed at 4°C overnight and cryoprotected for 2 days in 30 % sucrose. 40 µm coronal slices were cut using a sliding microtome. For immunostaining,

the floating brain sections were abundantly washed with phosphate-buffered saline (PBS) 1 x and then permeabilized with 0.3 % Triton X-100 in PBS for 1h at RT, and incubated with blocking solution (10 % goat-serum in PBS + 2 % Triton X 100) 2 hours at RT, and then incubated with primary antibodies **(Table 1)** in blocking solution overnight at 4 °C. When working with primary antibodies with mouse as host, an extra incubation before adding the primary antibody was performed with Mouse on Mouse (M.O.M.™) Blocking Reagent (Novus Biologicals) overnight at 4 °C. After washing three times with PBS, respective secondary antibodies were diluted in blocking solution and applied for 1 hour at RT: Alexa Fluor488, 555, 546, 647 (1:800) (Invitrogen). After two washes in PBS, sections were stained with Hoechst 33342 (1:2500, Thermo Fisher Scientific) for 10 minutes. Then, after a third wash, slices were mounted on microscope glass slides with ProLong Diamond mounting media (Thermo Fisher Scientific).

Image acquisition and analysis

Immunofluorescence images were acquired using a Leica TCS-SP5 confocal microscope under identical acquisition settings within each experiment. Analyses were performed in specific hippocampal subregions (CA1, CA3, and dentate gyrus), as specified for each marker and quantification in both hippocampi.

To minimize potential artifacts related to the injection procedure, image acquisition and quantification were performed in regions adjacent to but not directly overlapping with the injection site based on stereotaxic coordinates. Fields of view were selected in a blinded manner and all image analyses were conducted by an investigator unaware of experimental group allocation.

Quantifications were performed on merged z-stack projections using Fiji/ImageJ (NIH) software. Depending on the analysis, measurements were obtained either from the entire

image or from multiple regions of interest (ROIs) per image, which were averaged to yield a single value per image and subsequently per animal. For all analyses, the animal represented the biological replicate (n).

- *Tau pathology (AT8 and TauY9)*

For high-resolution tau quantification, AT8 and TauY9 immunoreactivity was analysed in CA1, CA3 and DG using a 40X objective. For each image, three regions of interest were manually defined within the relevant hippocampal subregion, and signal intensity was quantified and averaged per image. In analyses assessing global tau burden, AT8 and TauY9 immunoreactivity in hippocampus was obtained from calculating the mean from specific hippocampal subregions intensity.

- *Layer thickness*

For the measurements of the layer thickness of the cornu ammonis 1 (CA1) pyramidal cell layer and the dentate gyrus (DG) granule cell layer, hippocampal sections from similar coordinates were selected using a 40X objective. The thicknesses of the CA1 pyramidal cell layer and the DG granule cell layer were measured by drawing a scale perpendicular to the cell layer. Three to six different measurements per mouse were analysed and represented as mean thickness.

- *C1q and C1q / PSD95 associated puncta analyses*

Complement component 1q (C1q) immunoreactivity was analysed in both hippocampi using a 5x objective. For each image, mean intensity was normalized to the analysed area. C1q and postsynaptic density protein 95 (PSD95) associated puncta analyses was performed using a 63x objective and he Plug in “Puncta Analyzer” in ImageJ (https://imagej.net/contribute/citing) version 1.26 as reported in [13].

- *Microglial analysis*

Iba1 (Ionized calcium binding adaptor molecule 1) mean intensity was analysed in both

hippocampus and in the previously specified hippocampal regions using a 63x objective. A complementary analysis of CD68 (Cluster of Differentiation 68) restricted to regions defined by a mask of the Iba1 staining was done. CD68 signal was quantified within $Iba1^+$ cells using merged images. CD68-intensity was measured within the boundaries of individual $Iba1^+$ cells and averaged per image and per animal. At least 4 images per mouse were analysed. Additionally, using a 20x objective, the number of $Iba1^+$ cells were manually counted with the cell counter in Fiji software.

Microglial morphological score of the $Iba1^+$ cells in CA1 hippocampal region was performed following the protocol published in [19 ;13]. This semi-quantitative scoring approach has been widely used to classify microglial activation states and was used here as a complementary morphological readout alongside quantitative measurements of Iba1 and CD68. A score from 0 to 3 was given to microglia as follows: long processes with multiple branches (0); thicker processes with branches (1); thick retracted processes with few branches (2); round microglia without processes (3). Each microglial cell in an image received a morphology score, and the percent of microglia receiving a particular score was calculated for each image (number receiving score / total number of microglia x 100).

- *Astrocytic analysis*

Astrocytic reactivity was assessed using GFAP (Glial Fibrillary Acidic Protein) immunostaining by measuring mean intensity in both hippocampus and in the previously specified hippocampal regions using a 63x objective. For assessment of A1-like astrocytic activation, C3 (Complement 3) immunoreactivity was quantified within GFAP-positive cells using merged images. $C3^+$ signal was measured within GFAP-defined cellular boundaries and averaged per image and per animal. At least 4 images per mice were analysed.

For C3 analysis in $Iba1^+$ and $Iba1^-$ regions, at least three $Iba1^+$ and three $Iba1^-$ regions in the same image of the same hippocampus were assessed for C3 intensity. This procedure was

repeated in a total of two-to four images per mouse and results were represented as mean C3 intensity.

Behavioural tests

Behavioural data were analysed cross-sectionally by experimental time point. Mice were not subjected to repeated testing within the same behavioural paradigm across time points, and no repeated-measures statistical analyses were performed. At later stages of model characterization (28 and 56 dpi - days after injection-), T-maze testing was conducted immediately after completion of the NOR or OLT testing phase (T2), and two variants of the Y-maze were performed 24 hours later. These tasks evaluate related but distinct aspects of spatial and working memory and were not repeated across time points

- *Open Field Test (OFT)*

The Open Field test was employed to assess the locomotor activity of mice, as described in [20]. Each mouse was individually placed in a square box with 40 cm sides and observed while freely moving and exploring the environment; the square box was digitally divided into a 4 × 4 grid, creating 16 equal sections. Total distance travelled and mean speed were tracked for 5 minutes using AnyMaze software version 4.99 (Stoelting, Wood Dale, IL, USA).

- *Novel Object recognition Test (NOR)*

Recognition memory was assessed by performing the NOR test [21]. Briefly, on habituation day (T0), mice were individually placed into an open-field box of 40 × 40 × 40 cm and allowed to freely explore for 10 minutes; this recorded phase was used for the OFT. 24 hours later, during the training day (T1), animals were placed in the previous box and allowed to explore two identical objects for 8 min. On the following day, testing day (T2), to assess memory deficit, one object was replaced by a very different one (morphology, colour and texture) and

exploratory behaviour was recorded for 8 minutes. Due to the innate preference for novelty of the mice, mice without cognitive impairment will recognize the familiar object, spending most of the time at the novel object. Analysis was performed blinded by two independent observers using stopwatches. Manual scoring was preferred over automated tracking software as proximity-based detection may overestimate exploration when animals pass near the object without active interaction. Calculation of discrimination index (DI) was as follows: (time spent in new object − time spent in the old object) / (time spent in new object + time spent in the old object).

- *Object localization task (OLT)*

This was conducted in an empty box of 40 × 40 × 40 cm with visible spatial cues to evaluate spatial memory as described in [22]. T0 and T1 phases were performed mirroring the NOR test. However, during T2, mice were allowed to explore the box with one object moved to the opposite side. The preference for novelty was tested by determining the time spent in objects with novel and familiar locations. DI was calculated as previously mentioned evaluating novel and familiar locations. Objects and changes in object location were randomly determined and counterbalanced. Analysis was performed blinded by two independent observers using stopwatches. Mice were tested for behaviour in NOR test or OLT; never both tests were performed to the same mouse. *T-maze*

Short-term spatial memory was assessed in a T-maze (black, arms 30 x 10 cm) according to a protocol described before [23]. The T maze apparatus consists of two goal arms connected to a start arm to form a “T” shape, with a central partition in the upper middle of the “T” and two guillotine doors at the end of the right and left arms to confine the mice. Briefly, sample trials started when placing a mouse into the start arm (base of the T) to explore the maze with guillotine doors raised and the central partition placed. After an entry into a goal arm, a

guillotine door at the entrance of the goal arm was lowered, and the mouse was contained in that arm for 30 s. After this period, the test trial was initiated by placing the mouse in the start area with the guillotine doors opened and the central partition removed. A successful alternation was scored if the mouse chose to enter the previously non-visited goal arm. A total of seven completed trials were performed, distributed across two days (some hours before starting T0 of NOR/OLT and some hours after conducting T2) with at least 1 h retention interval in between. Each trial should take no more than 2 min. If animals performed for longer times, that trial was excluded. A minimum of five completed trials were used to calculate the percentage of correct alterations per mouse.

- *Y-maze*

Two variants of Y-maze (black, arms 30 x10 cm) were performed (**Figure 2F and G**). The following day after T-maze, Y-maze spontaneous alternation task (SAT), was performed to evaluate spatial working memory by placing the mice in the Y-shaped maze and they were recorded for 10 min as previously described [24]. A successful alternation was defined as consecutive entries into all three arms without returning to a previously visited arm. Thus, the maximum number of alternations was the total number of arm entries minus two, and the correct alternation percentage was calculated with the ANY-maze software as (actual alternations/maximum alternations) × 100. 24 h later, spatial reference memory, was also tested by placing the mice into the Y-maze with only two arms opened ('start' and 'familiar' arms) during 8 minutes of training. An opaque door blocked access to the third arm ('novel'). The test started after a 1 h retention time, when mice were placed again in the maze for 5 minutes with all arms accessible. Exploration was recorded with the ANY-maze software version 4.99 (Stoelting, Wood Dale, IL, USA) and percentage of time in the novel arm was calculated.

Statistical analysis

Animals were randomly allocated to experimental groups prior to the start of experiments. Investigators performing behavioural testing, image acquisition and quantification were blinded to group allocation. Inclusion criteria were defined a priori: only male mice of the appropriate age that successfully underwent stereotaxic surgery were included in the study. Animals were not excluded from analyses unless predefined humane endpoints or technical issues unrelated to experimental outcomes occurred (e.g., failed viral injection, surgical complications including reflux during injection or excessive surgical duration, or tissue damage preventing analysis). The animal was considered the experimental unit (biological replicate). Sample sizes were based on previous studies using similar models and endpoints rather than formal power calculations.

Prior to statistical testing, normality was assessed using the Shapiro Wilk test. Parameters with two groups were compared using unpaired, two-tailed t test. Post hoc multiple comparison tests were selected *a priori* based on the experimental design and the specific hypotheses tested. For model characterization experiments involving genotype and time as independent variables, two-way ANOVA followed by Sidak's multiple comparisons test was used to perform planned comparisons between control and AAV-tau mice at each time point. For therapeutic intervention experiments, where the primary objective was to compare multiple treatment groups against the AAV-tau disease group, one-way ANOVA followed by Dunnett's post hoc test was used. For insoluble AT8 quantifications, datasets were also assessed for normality. For monomeric AT8, which did not follow a normal distribution, non-parametric Kruskal-Wallis tests with Dunn's multiple comparisons post hoc were applied. Tukey's multiple comparisons test was applied only in experiments where all pairwise comparisons between groups were of interest (e.g., comparison of control, PLX-

treated males, and PLX-treated females).

The statistical test employed, and the number of independent replicates (n) used for each experiment are indicated in the respective figure legend. Statistical analyses were performed in GraphPad Prism 9.0.1.

RESULTS

Bilateral hippocampal AAV-hTau^{P301L} injection induces rapid tau propagation

Previously reported AD mouse models can take over a year to develop tau pathology and propagate across the different brain areas [25–27]. To shorten this time-window and accelerate the study on how microglial contributes to tau pathology we developed an inducible tauopathy mouse model, exhibiting rapid tau propagation using an AAV vector that expresses the transgene under the control of the neuron- specific synapsin-1 promoter (AAV2/6-SYN1) [28]. As the hippocampus is a brain region known to be most vulnerable in neurodegenerative diseases [29,30], we performed bilateral intrahippocampal (IHP) stereotaxic delivery of AAV particles containing the human tau protein with the P301L mutation, in WT male mice at three-to-five months of age (**AAV-hTau mice**). In parallel, the control group was injected with AAV particles containing innocuous GFP **(control mice).** At different days post-injection (dpi) (7, 14, 21, 28, and 56 dpi), mice were subjected to behavioural tests and samples were processed for biological studies (**Fig. 1A**).

First, we checked by western blot the differential expression of GFP in GFP-injected control mice, and AAV-hTau-injected mice at different time points. As expected, while GFP was only expressed in control mice, human tau protein detected by TY9 antibody (specific to human tau) was exclusively expressed in AAV-hTau mice at both time points analysed (14 and 28 dpi) (**Supplemental Fig. S1A**). Additionally, we stained brain sections to detect pathologically phosphorylated tau (p-tau) on Ser202 and Thr205 by AT8 antibody that

constitute the basis of Braak staging [31], to visualize how tau pathology develops across the hippocampus. Immunofluorescence analysis at final point (56 dpi) demonstrated widespread expression of human and p-tau across the whole hippocampus; most patent in dentate gyrus (DG) and CA3, and to a lesser extent in CA1 region (**Supplemental Fig. S1B**).

TY9 immunoreactivity and AT8 histological staining in the hippocampus was virtually undetectable at the tissue level in control animals **(Fig. 1B**). By contrast, low AT8-immunoreactive bands were still detectable by western blot in control hippocampal lysates, most likely reflecting endogenous murine tau phosphorylated at the AT8 epitope (**Figure 1F)**. In AAV-hTau mice, both histological and biochemical analyses showed a marked increase in TY9 and AT8-positive pathological tau species In AAV-hTau mice, although AT8 staining was not significant to control at 7 dpi, when sub-analysis by hippocampal region (CA1, DG and CA3) was performed, AT8 intensity resulted significant in DG and CA3, but not in CA1 **(Fig.1E)**. Interestingly, in AAV-hTau mice, staining of TY9 in the hippocampus at all time points showed a strong positive correlation with AT8 staining ($r=0.79$, $p<0.0001$), suggesting that the injected human P301L tau positively influenced its pathological phosphorylation **(Supplemental Fig. S1C)**.

To biochemically characterize p-tau in AAV-hTau mice at final point, sarkosyl-insoluble (SI) and sarkosyl-soluble (SS) fractions were analysed in hippocampal samples. Thereafter, pathological p-tau oligomers and monomers were evaluated by western blotting using AT8 antibody. Even though AT8 SS monomers showed a tendency to increase in AAV-hTau mice, we only found a significant increase in AT8 SI oligomers and monomers **(Fig. 1F- H)** indicating a greater amount of p-tau in a more insoluble fraction at final point. Altogether these results suggest that in AAV-hTau mice, p-tau pathology is established in the hippocampus as early as from 7 dpi and becomes insoluble to sarkosyl at final point.

AAV-hTau mice develop progressive reduction of hippocampal layer thickness and cognitive decline

Tau pathology leads to neurodegeneration and neuronal loss [32]. To elucidate whether neuronal loss was present during the progression of tauopathy in AAV-hTau mice, we measured the thickness of hippocampal layers that are typically affected in both animal models and patients during the course of tauopathies, such as the CA1 pyramidal cell layer and the DG granule cell layer [33–36]. AAV-hTau mice showed progressive thinness across hippocampal regions; CA1 was significantly thinner from 28 dpi while the DG granule cell layer from 21 dpi **(Fig. 2A, B and Supplemental Fig. S2A, B)**.

Thereafter, we assessed the impact of AAV-hTau injection on cognitive decline by performing different behavioural tasks. In the NOR test, control mice exhibited preference for the novel object over the familiar one, displaying a normal DI. As previously reported in other tauopathy models [16,37–39], AAV-hTau showed a time-dependent impairment in recognition memory, represented by a reduction in the DI, that was significant from 28 dpi **(Fig. 2C).** As AAV-hTau injections were performed in the hippocampus, we focused on hippocampus-dependent spatial and working memory evaluation by using four extra tests. We performed these behavioural tests at later stages, as recognition memory impairment was observed during the later time points analysed. Like in other tauopathy mouse models [37,40], AAV-hTau mice showed deficits in the object localization task (OLT), but contrary to recognition memory impairment, spatial memory impairment appeared at least one week earlier. Thus, from 21 dpi, AAV-hTau mice developed impairment in long-term spatial memory represented as a significantly reduction in the DI compared to controls. **(Fig. 2D).** In the T maze test, in agreement with previous reports in AD models [41–43] and with our NOR results, AAV-hTau mice from 28 dpi, failed to recognize the unexplored arm during the test time, indicative of reference and working memory deficits. On the contrary, control mice

exhibited a greater number of correct alternations as the natural tendency of mice is to alternate their choice of goal arm [23] **(Fig. 2E)**. In the Y-maze spontaneous alternation task, AAV-hTau mice exhibited reduced spontaneous alternation compared to controls **(Fig. 2F)**, indicating an impairment in spatial working memory as reported in other tauopathy models [38,44,45]). The Y-maze was also used to assess short-term spatial memory, based on their tendency to explore a novel environment. AAV-hTau mice showed a significantly reduced preference for the novel arm compared with controls **(Figure 2G).** Unlike previous cognitive tasks, significant differences in the Y maze were only observed at 56 dpi.

Lastly, locomotor activity was assessed by measuring mean speed and total distance travelled in the open filed test. The results showed that AAV-hTau mice exhibited hyperlocomotion (**Supplemental Fig. S2C)** consistent with findings in other tauopathy mouse models [46].

As thickness of the DG and CA1 neuronal layers has been reported to highly correlate with hippocampal volume [36], which in turn correlates with cognitive performance [47], we determined whether cognitive decline correlated with this parameter in our mice. Indeed, we observed a positive correlation between CA1 pyramidal and DG granule cell layer thickness, but also that both thickness measurements are good predictors of cognitive decline in our model, as both correlated with recognition memory measured as DI in the NOR test **(Supplemental Fig. S3A).** Focusing on AAV-hTau mice, the strongest correlation with cognitive impairment was found with the thickness of the DG region **(Supplemental Fig. S3B).**

We also correlated AT8 intensity in hippocampus with hippocampal layer thickness and memory impairment. As expected, Pearson's correlation analysis revealed a significant negative correlation between AT8 hippocampal staining with memory impairment, as well as

with DG layer thickness, when control and AAV-hTau mice were analysed together **(Supplemental Fig. S3C).**

C1q deposits in brain regions vulnerable to synapse loss at early stages of tauopathy

C1q, the initiator of the classical complement pathway, has been implicated in synapse loss in several neurodegenerative models [13,48–51]. Its accumulation at synapses seems to be more potently induced by tau pathology than amyloidosis [52]. In our tauopathy model, 14 dpi, we detected an increased C1q signal in the hippocampus, specifically in the molecular layer of the DG **(Fig. 3A, B),** a key localization for C1q deposition also observed by others [52,53]. In addition, previous reports demonstrated that C1q associates with p-tau-containing synapses [53]. In this line, we observed that C1q upregulation follows pathological p-tau accumulation in the hippocampus, as AAV-hTau mice showed a significant increase in hippocampal C1q immunoreactivity from 14 dpi **(Fig. 3A, D).** Among the different hippocampal regions, the DG exhibited the highest rise of C1q.

C1q colocalizes with synaptic markers, reactivating the complement-mediated pruning of synapses [13,50,53]. In our study, we observed a close apposition between C1q immunoreactivity and the postsynaptic protein marker PSD95 at 21 dpi, a key time point of elevated C1q in the hippocampus **(Fig. 3C, E)**. Further analysis indicated that the reduction in DG thickness had a strong correlation with the amount of C1q in hippocampus and negatively correlated with recognition memory (DI in the NOR test) **(Fig. 3F).** Overall, these results suggest a link between C1q, DG layer thickness and cognitive decline in our tauopathy model.

AAV-hTau mice present robust microglial activation in the hippocampus

To elucidate the interaction between activated microglia, tauopathy progression and

CA1 and DG layer thickness, we first characterized microglia. AAV-hTau mice showed an early increase in Iba1 and CD68 signal, with a peak reactive/phagocytic microglial profile between 14 and 21 dpi **(Fig. 4A, B and C)**. After this peak, Iba1/CD68 intensity declined, suggesting a dynamic and stage-dependent microglial response rather than a monotonic increase throughout disease progression.

We also examined the morphology of Iba1$^+$ cells following a similar protocol as in [13] **(Fig. 4D,** see materials and methods for scoring**)**. Although alterations in Iba1$^+$ cells started at 7 dpi, it was from 14 up to 21 dpi when AAV-hTau mice presented higher patterns of Iba1/CD68 positive cells across the hippocampus **(Fig. 4E)**.

Interestingly, hippocampal increase of CD68$^+$ cells correlated with the degree of DG thickness **(Fig. 4F)**. Similar observations were reported in other tauopathy models [54] and in humans [55]. This result suggests a possible link between reactive microglia (Iba1$^+$ and CD68$^+$ cells) and neurodegeneration, represented as a reduction in DG thickness. In fact, reduction in DG thickness and cognitive decline comes after the peak in CD68 induction.

In addition, given that microglia are a major source of C1q in the brain [56], we evaluated whether C1q was being upregulated during microglial activation, represented as an increase in CD68 in Iba1 positive cells. Indeed, we found a strong correlation (r=0.80; p=0.0004) between CD68 and C1q intensity **(Fig. 4G),** suggesting that in this model, microgliosis, and more specifically CD68$^+$ microglia in hippocampus, seem to contribute to the greater C1q accumulation in AAV-hTau mice which could, potentially, lead to subsequent synapse loss.

Induction of reactive astrocytes in the hippocampus of AAV-hTau mice

Activated microglia can drive astrocytes into a reactive state [9]. AAV-hTau mice

showed a clear increase in GFAP expression in the hippocampus from 21 dpi **(Fig. 5A, B, D),** but this increase was significantly reduced at the final point**.** Similar results were observed for GFAP$^+$ and C3$^+$ cells **(Fig. 5A, C).** Despite the reduction of these markers at final point (56 dpi) they remained higher compared to control, reflecting an increase of reactive astrocytes.

As induction of C3$^+$ astrocytes in the hippocampus appeared one week after microglial activation, we wondered if there could be a correlation between these two processes in AAV-hTau mice. Indeed, we found a positive correlation between the intensity of CD68 in Iba1$^+$ area, and C3 intensity in GFAP$^+$ area in AAV-hTau mice across all time points ($r = 0.49$, $p = 0.031$). However, if we only focus on the time points when both glial activations co-exist (from 21 to 56 dpi), this positive correlation became even stronger ($r = 0.70$, $p = 0.010$) **(Fig. 5E).** On the contrary, when correlation analysis was done between C3 intensity of astrocytes and the number of Iba1$^+$ cells, which is a hallmark of disease progression in mouse models of AD and tauopathies, we did not find any significant correlation **(Fig. 5F)**. These findings suggest that the reactive state of microglia, rather than their proliferation, relates with C3$^+$ astrocyte in AAV-hTau mice.

Evaluation of the impact of microglia at different stages of tauopathy progression.

Having established the timeline of pathological events following AAV-hTau induction in our model (**Fig. 6A**), we developed different microglial depletion strategies to investigate the impact of microglial on these processes. Apart from the control and AAV-hTau groups, we generated five additional AAV-hTau groups treated with PLX5622 in chow at critical time-points as indicated in **Fig. 6B**; all groups were maintained until 56 dpi. The **AAV-hTau PLX d-7** group was the only one in which microglia was depleted before inducing tauopathy; this is, 7 days before AAV-hTau injection and maintained throughout the entire period. In the rest

of AAV-hTauPLX groups, PLX5622 was introduced with a disease-modifying purpose effect once tauopathy was manifested and during key points of disease progression as follows: (i) 7 days dpi, when microglia starts to activate **(AAV-hTau PLX d7)**; (ii), 14 dpi, when microglia is clearly activated **(AAV-hTau PLX d14),** but before inducing reactive astrocytes, reduction in hippocampal layer thickness and cognitive decline; (iii) 21 dpi, microglia is activated, reactive astrocytes are induced, and first signs of neurodegeneration appear **(AAV-hTau PLX d21)** and (iv) 28 dpi, when there is notable and evident reduction of hippocampal layer thickness and cognitive decline **(AAV-hTau PLXd28).**

As CSF1R inhibitors can produce a sex-dependent microglial depletion efficiency in mice [57], we examined this effect with our CSF1R inhibitor PLX5622. Control male mice showed higher microglial reduction (~90%) than females (~60%) when treated for 14 days with the same chow **(Fig. 6C, D).** Therefore, to ensure maximum microglial depletion and assess their contribution to tau pathology and progression, we only used male mice. The number of Iba1$^+$ cells in AAV-hTau mice was significantly reduced in all PLX treated groups (**Fig. F)** although microglial depletion was not as effective as in non-injected animals (**Fig. 6D**). Because Iba1 labels both resident microglia and other CNS-associated myeloid cells, we cannot exclude that some of the residual Iba1-positive cells after PLX5622 represent infiltrating macrophages/monocytes or other non-parenchymal myeloid cells rather than incompletely depleted resident microglia. This possibility may be particularly relevant in the context of local stereotaxic hippocampal injection, which is known to induce a tissue inflammatory response [58 ; 59].

Microglial depletion during a critical time window of tauopathy progression reverses cognitive impairment and reduction of CA1/DG layer thickness

From a clinical perspective, prevention of cognitive decline is our major readout after

using the different microglial depletion strategies in our tauopathy model. Except for the AAV-hTau PLXd28 group, all PLX5622-treated mice significantly improved their cognitive performance compared to AAV-hTau mice in the T-maze **(Fig. 7A),** OLT **(Fig. 7B)** and NOR test **(Fig. 7C)**, indicating an improvement in working, reference and spatial memory. Interestingly, in all AAV-hTau PLX groups, the hyperlocomotion activity observed in AAV-hTau mice was prevented by microglia ablation **(Supplemental Fig. S4),** reinforcing a positive drug effect**.**

We next evaluated the thickness of CA1 pyramidal and DG granule cell layers. Mirroring the results in the memory tests, except for AAV-hTau PLX d28 mice, all AAV-hTau PLX groups showed higher layer thickness in CA1 **(Fig. 7D, E)** and DG **(Fig. 7F, G)** compared to AAV-hTau group. As both CA1 pyramidal and DG granule cell layer thickness measurements were good predictors of cognitive decline, we performed the same correlations in AAV-hTau PLX groups. Consistent with our previous findings, not only CA1 but also DG thickness positively correlated with cognition measured by the DI in the NOR test (**Fig. 7H, I**).

Microglial activation is associated with p-tau pathology

Previous studies in mouse models of tauopathies reported a strong link between microglia activation and the development of tau pathology [60–63] or *vice versa* [64,65]. Also, microglial activation has shown to promote tau phosphorylation by activating tau kinases via IL-1 signalling [66,67]. In addition, activated microglia can also trigger neurodegeneration that leads to secondary tau hyperphosphorylation and aggregation as a consequence of neuronal injury [65]. We therefore analysed tau pathology in brains of AAV-hTau PLX5622-treated mice. Whereas TY9 and AT8 staining were virtually undetectable in control brains at 56 dpi, AAV-hTau mice showed a significant increase in both immunoreactivities in the hippocampus

(Fig. 8A-C). Human TY9 tau levels between PLX5622 AAV-hTau-injected groups were comparable, mice treated with PLX5622 at all time points blocked the progression of p-tau as represented by the significant reduction of AT8 immunoreactivity **(Fig. 8A-C).**

Furthermore, p-tau levels in soluble and insoluble sarkosyl fractions were analysed by western blot using AT8. Consistent with our previous results, we only found a significant increase in AT8 SI, both oligomers and monomers **(Fig. 8D, E)**. Surprisingly, in all AAV-hTau PLX5622-treated mice, the elevation of AT8 SI oligomers were significantly reduced. Importantly, no statistical comparisons were performed between PLX-treated groups, and therefore apparent differences between regimens (e.g., d28) should not be interpreted as reflecting differential efficacy. In agreement with our previous results, we did not find a significant increase in AT8 SS in AAV-hTau mice and consequently PLX5622-treated groups did not show differences in comparison with AAV-hTau group (**Fig. 8F, G**).

While the insoluble monomeric fraction of AT8 shows high variability, the immunofluorescence data clearly demonstrate a consistent increase in AAV-hTau mice, which is significantly reduced upon PLX treatment. The oligomeric fraction shows a similar trend and is statistically confirmed by parametric analysis. Overall, the concordance across independent readouts supports the conclusion that PLX reduces tau pathology.

C1q reduction in AAV-hTau mice after microglia depletion

We previously detected a strong correlation between CD68 and C1q intensity, supporting the idea that activated microglia might contribute to the greater deposition of C1q in tauopathy. Consistent with the current and previous studies [53,68], C1q signal was highly intense in the DG molecular layer in AAV-hTau mice **(Fig. 9A).** However, as reported in an AD model with combined Aβ-tau pathology [68], the elevation in C1q in hippocampus in AAV-

hTau mice was significantly reduced following microglia depletion **(Fig. 9A, B).** Interestingly, we found a significant negative correlation between C1q deposition in hippocampus and cognitive performance in the NOR test **(Fig. 9C)**. Overall, these results suggest that the increase in hippocampal C1q was microglia-dependent.

AAV-hTau-PLX5622 treated mice did not show a clear blockade of C3$^+$ reactive astrocytes

To determine whether elimination of microglia before, shortly, or even late after its activation results in suppression of reactive astrocyte conversion *in vivo*, we characterized the population of astrocytes in control, AAV-hTau, and AAV-hTau-PLX5622 treated mice. At 56 dpi, AAV-hTau mice had increased levels of GFAP and the reactive astrocyte marker C3 in the hippocampus **(Fig. 10A, C).** Interestingly, the absence of microglia did not affect total number of astrocytes in hippocampus, measured as number of GFAP$^+$ cells **(Fig. 10B)** in AAV-hTau mice**.** Also, none of the AAV-hTau-PLX5622 treated groups showed statistical differences in C3 intensity in comparison with AAV-hTau **(Fig. 10C);** however, when microglial depletion was induced before the appearance of C3$^+$ astrocytes (AAV-hTau PLX7d and AAV-hTau PLX14d), there was a clear trend towards reduction of astrocyte reactivity. In fact, both groups showed significant differences against AAV-hTau group when compared with a t-test ($p = 0.021$ and $p = 0.0090$, respectively). These results, although not statistically significant by the selected test, clearly demonstrate a different behaviour over astrocytes reactivity among AAV-hTau-PLX5622 treated groups depending on the time point when microglia were depleted and its state.

As the total number of astrocytes remained unchanged among groups, microglia elimination seems to modulate astrocyte reactivity but not its proliferation. Despite the supposedly destructive A1 astrocyte phenotype, our previous results on C3 intensity at final

point in AAV-hTau PLX mice, do not show a clear linear relationship between C3 intensity in astrocytes and cognition. Consistent with this observation was the lack of correlation between de DI in the NOR test and the intensity of C3 in GFAP$^+$ astrocytes in the AAV-hTau PLX treated groups **(Fig. 10D).** These results support the fact that C3$^+$ astrocytes in our tauopathy model do not seem to directly regulate neurodegeneration.

Differential localization of C3$^+$ astrocytes with Iba1$^+$ cells

A potential explanation for the trend rather than the expected full blockade of C3$^+$ astrocytes induction following microglia depletion could be PLX5622´s efficiency. In fact, similar results were obtained in an LPS mouse model, where the small subset of microglia that remained after CSF1R inhibitor treatment mounted a response to LPS still producing C3$^+$ astrocytes [9]. As our efficiency in microglia depletion was around 90 % in AAV-hTau mice**,** we tested this hypothesis in our model, by immunostaining mouse brains with C3 and Iba1. We then evaluated the intensity of C3 in two types of regions in the same hippocampus: regions completely devoid of Iba1$^+$ cells (Iba1) and regions with still surviving Iba1$^+$ cells **(Fig. 10E).** The presence of surviving Iba1$^+$ cells in all PLX5622-treated AAV-hTau mice was associated with higher levels of C3 next to them in comparison with negative regions for Iba1 in the same hippocampus **(Fig. 10E, F),** indicating that proximity of Iba1$^+$ cells seems to play an important role for astrocyte reactivity.

DISCUSSION

In this study, we investigated the role of microglia across the progression of tauopathy using a rapid inducible AAV-hTauP301L model combined with temporally controlled depletion using the CSF1R inhibitor PLX5622. Our results show that microglial depletion at different

disease stages differentially impacts tau pathology, glial responses, hippocampal layer integrity, and cognitive performance.

The AAV-hTauP^{301L} model offers several advantages over traditional transgenic systems, allowing temporal and spatial control of tau expression and enabling rapid disease progression. In this model, pathological tau phosphorylation precedes complement activation, glial reactivity, structural alterations in hippocampal layers, and cognitive impairment, broadly consistent with previous reports [52,59]. While this system introduces some experimental artificiality, it provides a tractable framework for dissecting temporal relationships between pathological events.

Microglial activation emerged as an early feature, with increased Iba1 and CD68 signals peaking between 14 and 21 dpi. Importantly, the subsequent decline in Iba1/CD68 intensity despite ongoing disease progression should not be interpreted as reduced microglial involvement. Rather, it likely reflects a transition from an early reactive/phagocytic state to a later dysfunctional or hypofunctional phenotype, as described in tauopathy models [80] and supported by previous studies [69–71]. In this context, early microglial activation may initiate downstream pathogenic cascades, including complement deposition and astroglial reactivity, whose consequences persist beyond the peak of CD68 expression.

Consistent with this, we observed early and robust C1q deposition, particularly in regions with prominent tau pathology. Given that microglia are a major source of C1q [75], the reduction in C1q following PLX5622 treatment is expected. Importantly, we limit our interpretation to this well-established relationship. While C1q has been implicated in synapse elimination [13,76,77], synaptic alterations were not directly measured in this study, and therefore any role in synapse loss should be considered hypothetical. Supporting a functional link, we observed a significant negative correlation between hippocampal C1q deposition and cognitive performance in the NOR test, suggesting that increased C1q may be associated

with impaired function in this model.

Previous studies have already shown that microglia contribute to tau pathology and neurodegeneration [72,73], that complement C1q is involved in tau-related synaptic injury [74], and that activated microglia can induce C3/A1-like reactive astrocytes [75]. The main contribution of our study is the temporal integration of these events within a single inducible model, together with behavioral outcomes and stage-specific microglial depletion. Given that microglial depletion is achieved rapidly after PLX5622 administration and was sustained in all treatment groups, the observed differences are more likely to reflect the stage at which treatment was initiated rather than differences in depletion efficacy. Within this context, our data support a stage-dependent therapeutic effect.

Microglial depletion also reduced p-tau accumulation, particularly insoluble AT8-positive species, supporting a role for microglia in shaping tau pathology. However, the relationship between tau burden and functional impairment is not necessarily linear, and it remains unclear whether neuroprotection is primarily driven by reduced tau pathology or by direct attenuation of microglia-mediated neurotoxicity.

Microglia–astrocyte crosstalk was also evident in this model. C3-positive astrocytes appeared after microglial activation and C1q deposition, consistent with previous reports [9,51,76,82]. Despite a trend toward reduced astrocytic C3 reactivity after PLX5622 treatment, global C3 signal was not significantly reduced at the endpoint. Therefore, our data do not support a simple linear relationship between total residual Iba1$^+$ cell number and total C3$^+$ astrocyte burden. Instead, we observed a more local and state-dependent association: astrocytic C3 intensity correlated with microglial CD68 reactivity, but not with Iba1$^+$ cell number, and was higher in regions containing residual Iba1$^+$ cells compared to adjacent Iba1$^-$ areas. Thus, residual microglia may contribute to the local induction and/or maintenance of astrocytic C3 reactivity, but they are unlikely to fully explain the persistence of global C3

signal after PLX5622 treatment. Therefore, our data do not allow us to determine the mechanisms underlying the persistence of C3 signal after microglial depletion.

Although reductions in C1q deposition and reactive astrocytes correlate with neuroprotection, these parameters were not independently manipulated and therefore cannot be assigned a causal role.

Despite prior reports of neuroprotective effects of CSF1R inhibition [17,87–89], our study extends these findings by integrating behavioral outcomes and temporal intervention strategies. However, differences across studies likely reflect variability in model systems, disease kinetics, and depletion paradigms.

Several limitations should be considered. First, Iba1 does not distinguish resident microglia from infiltrating monocyte-derived macrophages, particularly in the context of stereotaxic injection, and therefore the cellular identity of residual Iba1$^+$ cells after PLX5622 cannot be conclusively determined. Second, only male mice were used. In animal models, microglial depletion is less effective in females [76] and our study, whereas women show increased susceptibility to tau accumulation and cognitive decline [77–79], suggesting that therapeutic responses may be sex-dependent. Finally, although microglial depletion shows promise in preclinical models, long-term suppression of brain innate immunity raises safety concerns, including potential infection risk and compensatory infiltration of peripheral myeloid cells [92]. Therefore, defining optimal timing and potentially combining transient depletion with repopulation strategies may be required for clinical translation.

CONCLUSIONS

1. Bihippocampal delivery of AAV-hTau^{P301L} in mice provides a model that recapitulates key hallmarks of tauopathy such as hyperphosphorylation of tau, complement activation, glial reactivity, structural alterations in hippocampal layers, and cognitive

impairment.

2. Microglial activation is an important contributor to structural changes in hippocampal layers and cognitive decline in the context of tau pathology.
3. Microglial depletion may confer neuroprotection through mechanisms associated with reduced levels of insoluble p-tau oligomers, partial inhibition of $C3^+$ astrocyte induction, and attenuation of microglial reactivity.

Overall, these findings support a stage-dependent therapeutic window in which microglia-targeted interventions may modify disease progression, particularly before overt neurodegeneration is established.

FIGURE LEGENDS

Figure 1. Tau pathology develops in the hippocampus of AAV-hTau mice from 7 dpi. **(A)** Schematic representation of the experimental design: AAV-GFP (Control) and AAV-hTau injected groups (hTau); coordinates of bilateral IHP injection, and time points selected for biological and behavioural analysis. **(B)** Representative images of TY9 and AT8 staining in CA3. Insets show images at a higher magnification. Scale bar: 50 μm (40X). Quantification of **(C)** TY9 and **(D)** AT8 intensity in the hippocampus in control (n = 4-5) and AAV-hTau (n = 4-8) mice. **(E)** Quantification of AT8 intensity in CA1, CA3 and DG in control (n=4) and AAV-hTau (n=5) mice 7 dpi. **(F)** Representative images and quantification of AT8 SS **(G)** and SI **(H)** tau oligomers and monomers from hippocampal lysates in control (n =10-12) and AAV-hTau (n = 9-12) mice. Ponceau staining was used as loading control. Data are presented as mean ± SEM. Significance was determined by two-way ANOVA followed by Šidák's multiple comparisons or unpaired two-tailed Student's t-test. *$p < 0.05$; **$p < 0.01$; ***$p < 0.001$; ****$p < 0.0001$. *Control (C); AAV-hTau (T or hTau); sarkosyl-insoluble (SI) and sarkosyl-soluble fractions (SS); days post-injection (dpi); Dentate Gyrus (DG).*

Figure 2. AAV-hTau mice develop a time-dependent decrease in hippocampal CA1 and DG layer thickness and cognitive function. (A) Representative images of CA1 and DG 56 dpi; CA1 layers shown are the pyramidal cell layer (PCL), stratum radiatum (SR) and stratum lacunosum-moleculare (SLM). Dentate gyrus (DG) regions include the granule layer (GL), polymorphic layer (PM) and ML (molecular layer). Scale bars: CA1 images 30 μm (40X); DG images 50 μm (40X). **(B)** Thickness quantification of CA1 pyramidal neuronal layer and DG granular cell layer in control (n = 4-8) and AAV-hTau (n = 5-9) mice at different dpi. **(C)** Schematic representation of the NOR test and quantification of the DI in control (n = 4-11)

and AAV-hTau (n= 6-17) mice. **(D)** Schematic representation of the OLT and quantification of the DI in control (n = 7-15) and AAV-hTau (n =10-16) mice. **(E)** Schematic representation of the T maze and quantification of the percentage of correct alternations in control (n = 9-18) and AAV-hTau (n = 13-23) mice. **(F)** Schematic representation of the Y-maze SAT and percentage of correct alternations in control and AAV-hTau mice. **(G)** Schematic representation of the short-term memory Y test and quantification of the percentage of time spent in the novel arm in control and AAV-hTau mice. Data are presented as mean ± SEM in **(B-E)** and individual values in **(F-G).** Significance was determined by two-way ANOVA followed by Šidák's multiple comparisons. *p < 0.05; **p < 0.01; ***p < 0.001; ****p < 0.0001. *AAV-hTau (hTau); Training Day (T1); Testing Day (T2); Novel object recognition (NOR); Object localization task (OLT).*

Figure 3. C1q deposition in hippocampus of AAV-hTau mice. (A) Representative confocal images showing C1q at different dpi; Scale bar: 500 µm (5X). **(B)** Images at 21 dpi at a higher magnification; DG regions represented include the granule layer (GL) and ML (molecular layer). **(C)** Images of C1q in close apposition to PSD95-positive synaptic puncta in the hippocampus. **(D)** Quantification of C1q at different dpi in the hippocampus. **(E)** Quantification of C1q apposition with PSD95 in control (n = 4) and AAV-hTau (n = 5) mice 21 dpi. Scale bar: 5 µm (63X). Data are presented as mean ± SEM. Significance was determined by two-way ANOVA followed by Šidák's multiple comparisons or unpaired two-tailed Student's t-test. *p < 0.05; **p < 0.01; ****p < 0.0001. **(F)** Relationship between C1q intensity in hippocampus (x axis), DG granule cell layer thickness (y axis), and DI from NOR test. Each dot represents an individual mouse, the dot color indicates the experimental group, and the dot size corresponds to increased values DI (all data previously reported in Fig. 2). Significant Pearson's correlations were observed between C1q intensity to DI (r = -0.37, *p < 0.05) and

between DG layer thickness and DI (previously reported in Fig 2). A strong negative correlation was observed between C1q intensity and DG layer thickness (r = -0.74, *****p < 0.0001). The same correlations were also performed in AAV-hTau mice group alone: C1q vs DI (r = -0.11, p = 0.67), C1q vs DG layer thickness (r = -0.68, *****p < 0.0001). *AAV-hTau (hTau); Dentate Gyrus (DG); days-post injection (dpi).*

Figure 4. Robust activation of CD68$^+$ microglia from 14 dpi in AAV-hTau mice. (A) Representative images and quantification of **(B)** Iba1 and **(C)** CD68 intensity in Iba1$^+$ area in control (n = 4) and AAV-hTau (n = 5) mice. Scale bar: 500 μm (20X, mosaic). Insets show images of 14 dpi at a higher magnification Scale bar: 25 μm (63X). **(D)** Representative images and **(E)** quantification of the morphology score of Iba1$^+$ cells in CA1 hippocampal region from 7 to 21 dpi in control (n = 4) and AAV-hTau (n = 5) mice. Scale bar: 10 μm (63X). Data are presented as mean ± SEM. Significance was determined by two-way ANOVA followed by Šidák's multiple comparisons or unpaired two-tailed Student's t-test. *p < 0.05; **p < 0.01; ***p < 0.001; ****p < 0.0001. **(F)** Correlation between CD68 intensity in Iba1$^+$ area in hippocampus and DG granular layer thickness (n = 14) or **(G)** C1q intensity (n = 15) in AAV-hTau mice. Pearson correlation analysis, r = -0.54, *p < 0.05, and r = 0.80, ***p < 0.001, respectively (two-tailed). *Days post-injection (dpi); AAV-hTau (hTau); Dentate Gyrus (DG).*

Figure 5. C3 intensity in GFAP$^+$ astrocytes increases in AAV-hTau mice from 21 dpi. (A) Representative images and quantification of **(B)** GFAP and **(C)** C3 intensity in GFAP$^+$ area in control (n = 4 - 7) and AAV-hTau (n = 5 - 7) mice. Scale bar: 500 μm (20X, mosaic). Insets show images of 21 dpi at a higher magnification Scale bar: 25 μm (63X). **(D)** Representative images and quantification of GFAP expression in hippocampal homogenates. Data are presented as mean ± SEM. Significance was determined by two-way ANOVA

followed by Šidák's multiple comparisons or unpaired two-tailed Student's t-test. *p < 0.05; **p < 0.01; ***p < 0.001; ****p < 0.0001. **(E)** Correlation between C3 intensity in GFAP$^+$ area in hippocampus and CD68 intensity in Iba1$^+$ area in hippocampus (reported in Fig. 4) (n = 12) or **(F)** number of Iba1$^+$ cells / FOV in hippocampus (n = 12) in AAV-hTau mice. Pearson correlation analysis, r = 0.70, *p < 0.05, and r = 0.022, p = 0.945, respectively (two-tailed). *Days post injection (dpi); control (C); AAV-hTau (T or h-Tau); field of vision (FOV).*

Figure 6. Experimental design and characterization of the microglial depletion strategy. (A) Timeline of tau-related pathological events in mice after induction of tauopathy. **(B)** Experimental design showing treatments and experimental groups: control, AAV-hTau, and AAV-hTau groups treated with PLX5622 (hTau PLX) at different time points (7 days before AAV-hTau injection, and 7, 14, 21 and 28 dpi). Unless PLX5622 chow is represented in the scheme, mice are fed with control chow. **(C)** Images and **(D)** quantification of Iba1 staining in hippocampus in male and female mice after 14 days of control diet, or PLX5622 diet. Insets show images of Iba1 staining after PLX5622 diet at a higher magnification Scale bar: 75 μm (20X). Scale bar: 25 μm (63X). Data are presented as mean ± SEM, and sample sizes (mice) are indicated by dots within the figure panels. Significance was determined by one-way ANOVA with Tukey's post hoc test. ****p < 0.0001 compared to control diet; $^{\#\#}$p<0.01 comparison between sexes. **(E)** Representative images of Iba1 staining in hippocampus in control, AAV-hTau and AAV-hTau PLX groups (PLX d-7, PLX d7, PLX d14, PLX d21, PLX d28) 56 dpi. Scale bar: 25 μm (63X) and their **(F)** quantification**.** Data are presented as mean ± SEM, and sample sizes (mice) are indicated by dots within the figure panels. Significance was determined by one-way ANOVA with Dunnett's post hoc test. ****p < 0.0001. *Days post-injection (dpi); AAV-hTau (h-Tau).*

Figure 7. Microglial depletion before overt neurodegeneration preserves CA1 and DG thickness and correlates with improved cognitive behaviour in the setting of pure tauopathy. (A) Analysis of the percentage of correct alternations in the T-Maze, **(B)** DI´s in the OLT and **(C)** NOR test in control, AAV-hTau and AAV-hTau PLX groups (PLX d-7, PLX d7, PLX d14, PLX d21, PLX d28) 56 dpi. Data are presented as mean ± SEM, and sample sizes (number of mice) are indicated by dots within the figure panels. **(D)** Representative images and **(E)** thickness quantification of CA1 pyramidal neuronal layer. **(F)** Representative images and **(G)** quantification of DG granular cell layer in control, AAV-hTau mice, and AAV-hTau PLX groups 56 dpi. Scale bars: CA1 images 30µm (40X); DG images 50 µm (40X). Correlation between DI in the NOR test and **(H)** CA1 pyramidal neuronal layer thickness or **(I)** DG granular cell layer thickness in AAV-hTau PLX mice 56 dpi. Pearson correlation analysis, r = 0.48, *p < 0.05, and r = 0.43, *p < 0.05, respectively (two-tailed). Data are presented as mean ± SEM, and sample sizes (mice) are indicated by dots within the figure panels. Significance was determined by one-way ANOVA with Dunnett's post hoc test. *p < 0.05; **p < 0.01; ***p < 0.001; ****p < 0.0001. *Discrimination index (DI); days post-injection (dpi); AAV-hTau (hTau); dentate gyrus (DG); granule layer (GL).*

Figure 8. Microglial contribution to p-tau pathology. (A) Representative images of CA1 region and quantification of **(B)** TY9 and **(C)** AT8 intensity in the hippocampus in control, AAV-hTau and AAV-hTau PLX groups (PLX d-7, PLX d7, PLX d14, PLX d21, PLX d28) 56 dpi. Scale bars: 25 µm (40X). **(D, F)** Representative images and quantification of **(E)** AT8 SI and **(G)** AT8 SS oligomers and monomers from hippocampal lysates of control, AAV-hTau mice, and AAV-hTau PLX groups 56 dpi. Ponceau staining was used as loading control. Data are presented as mean ± SEM, and sample sizes (mice) are indicated by dots within the figure panels. Significance was determined by one-way ANOVA with Dunnett's post hoc

test or Kruskal-Wallis test with Dunn's multiple comparisons post hoc for SI monomers. *p < 0.05; **p < 0.01; ***p < 0.001; ****p < 0.0001. *Days post-injection (dpi); AAV-hTau (hTau); sarkosyl-insoluble (SI) and sarkosyl-soluble fractions (SS).*

Figure 9. C1q in the hippocampus was reduced in AAV-hTau PLX5622-treated mice. **(A)** Representative images and **(B)** quantification of C1q staining in hippocampus in control, AAV-hTau mice, and AAV-hTau PLX groups (PLX d-7, PLX d7, PLX d14, PLX d21, PLX d28) 56 dpi. Scale bars: 500 µm (5X). **(C)** Correlation between DI in the NOR test and C1q intensity in hippocampus in AAV-hTau PLX mice 56 dpi Pearson correlation analysis, r = -0,53, **p < 0.01 (two-tailed). Data are presented as mean ± SEM, and sample sizes (mice) are indicated by dots within the figure panels. Significance was determined by one-way ANOVA with Dunnett's post hoc test. *p < 0.05; ***p < 0.001; ****p < 0.0001. *Days post-injection (dpi); AAV-hTau (h-Tau).*

Figure 10. AAV-hTau PLX groups did not show a clear block of C3$^+$ reactive astrocytes, but C3$^+$ astrocytes were closely associated with surviving microglia. (A) Representative images and quantification of number of **(B)** GFAP$^+$ cells and **(C)** C3 intensity in GFAP$^+$ area in the hippocampus in control, AAV-hTau mice, and AAV-hTau PLX groups (PLX d-7, PLX d7, PLX d14, PLX d21, PLX d28) 56 dpi. Scale bars: 50 µm (63X). **(D)** Correlation between DI in the NOR test and C3 intensity in GFAP$^+$ area in hippocampus in AAV-hTau PLX mice 56 dpi. Pearson correlation analysis, (r = -0.14, p = 0.50) (two-tailed). **(E)** Representative images and **(F)** quantification of C3 intensity in regions Iba1$^+$ (blue) and Iba1$^-$ (black) in the same hippocampus in hTau PLX groups 56 dpi. Data are presented as individual values in Iba1$^+$ and Iba1$^-$ regions (n = 5-7 mice). Significance was determined by the unpaired two-tailed Student's t-test. *p < 0.05; **p < 0.01. Data are presented as mean ± SEM, and sample

sizes (mice) are indicated by dots within the figure panels. Significance was determined by one-way ANOVA with Dunnett's post hoc test or unpaired two-tailed Student's t-test. *p < 0.05; **p < 0.01. *Field of vision (FOV); days post-injection (dpi); AAV-hTau (h-Tau)*

SUPPLEMENTARY FIGURE LEGENDS

Supplementary figure 1. Characterization of the humanized tauopathy *in vivo* mouse model. (A) Representative images of protein expression levels of TY9 and GFP from hippocampal lysates in control (n = 3) and AAV-hTau (n = 4) mice 14 and 28 dpi. **(B)** Representative images of GFP, TY9 and AT8 intensity in brain slices of control and AAV-hTau mice 56 dpi. Scale bar: 500 μm (5X). **(C)** Correlation between TY9 and AT8 intensity in hippocampus in AAV-hTau (n = 26) mice. Pearson correlation analysis, r = 0.79, ****p < 0.0001 (two-tailed). *days post-injection (dpi); AAV-hTau (h-Tau)*

Supplementary figure 2. Time-dependent reduction of CA1 and DG thickness and increase in locomotor activity y h-Tau mice. Representative Hoechst-stained images of **(A)** CA1 and **(B)** dentate gyrus (DG) in control and hTau mice at 7, 14, 21 and 28 dpi. The CA1 layer shown is the pyramidal cell layer (PCL), and the DG layer represented is the granule layer (GL) Scale bars: CA1 images 30 μm (40X); DG images 50 μm (40X). **(C)** Locomotor activity in the openfield test and quantification of the distance travelled and mean speed 28 and 56 dpi in control (white bars) and hTau (blue bars) mice. Data are presented as mean ± SEM. Significance was determined by two-way ANOVA followed by Šidák's multiple comparisons. *p < 0.05. *Days post injection (dpi); AAV-hTau (h-Tau)*

Supplementary figure 3. Strong correlation between DG layer thickness and recognition memory impairment. (A) Relationship between DG granule cell layer thickness (x axis), CA1 pyramidal cell layer thickness (y axis), and DI from the NOR test. Each dot represents an individual mouse, the dot colour indicates the experimental group, and the dot size corresponds to increased values of DI (all data have been previously reported in Fig. 2). Significant Pearson's correlations were observed between DG layer thickness to DI ($r = 0.70$, ****$p < 0.0001$) and between CA1 layer thickness and DI ($r = 0.41$, *$p < 0.05$). A positive correlation was observed between thickness of both layers ($r = 0.64$, *****$p < 0.0001$). The same correlations were also performed in AAV-hTau mice group alone: DG thickness vs DI ($r = 0.62$, **$p < 0.01$), DG *vs* CA1 thickness ($r = 0.62$, ***$p < 0.001$), CA1 thickness *vs* DI ($r = 0.38$, $p = 0.187$). **(B)** Correlation between DG thickness layer and DI in AAV-hTau mice alone ($n = 18$). Pearson correlation analysis, $r = 0.62$, **$p < 0.01$ (two-tailed). **(C)** Relationship between DG granule cell layer thickness (x axis), DI from NOR test (y axis), and AT8 intensity in hippocampus. Each dot represents an individual mouse, the dot colour indicates the experimental group, and the dot size corresponds to increased values of AT8 intensity in hippocampus (all data previously reported in Fig. 1 and 2). Significant Pearson's correlations were observed between DG layer thickness and AT8 intensity ($r = -0.49$, **$p<0.01$) and, between DI and AT8 intensity ($r = -0.62$, **$p < 0.01$). The same correlations were also performed in AAV-hTau mice group alone: DG thickness *vs* AT8 intensity ($r = 0.078$, $p = 0.720$), DI *vs* AT8 intensity ($r = -0.49$, $p = 0.066$). *Dentate Gyrus (DG); AAV-hTau (h-Tau)*

Supplementary figure 4. Microglia depletion prevents hyperlocomotion in the Open field test. Analysis of the mean speed in the OFT in AAV-hTau mice, and AAV-hTau PLX groups (PLX d-7, PLX d7, PLX d14, PLX d21, PLX d28) 56 dpi. Data are presented as mean

± SEM, and sample sizes (number of mice) are indicated by dots within the figure panels. Significance was determined by one-way ANOVA with Dunnett's post hoc test. ****p < 0.0001, ## p<0.01. *Days post-injection (dpi); AAV-hTau (h-Tau)*

Supplementary file 5: uncropped Gels and Blots images of: (**A)** Figure 1F, Figure 8F and 8D; (**B)** Figure 5D and (**C)** Sup. Figure 1.

BIBLIOGRAPHY

1. Chen Y, Yu Y. Tau and neuroinflammation in Alzheimer's disease: interplay mechanisms and clinical translation. J Neuroinflammation. 2023;20:165. https://doi.org/10.1186/s12974-023-02853-3
2. Leyns CEG, Holtzman DM. Glial contributions to neurodegeneration in tauopathies. Mol Neurodegener. 2017;12:50. https://doi.org/10.1186/s13024-017-0192-x
3. Didonna A. Tau at the interface between neurodegeneration and neuroinflammation. Genes Immun. 2020;21:288–300. https://doi.org/10.1038/s41435-020-00113-5
4. Nayak D, Roth TL, McGavern DB. Microglia Development and Function. Annu Rev Immunol. 2014;32:367–402. https://doi.org/10.1146/annurev-immunol-032713-120240
5. Colonna M, Butovsky O. Microglia Function in the Central Nervous System During Health and Neurodegeneration. Annu Rev Immunol. 2017;35:441–68. https://doi.org/10.1146/annurev-immunol-051116-052358
6. McQuade A, Blurton-Jones M. Microglia in Alzheimer's Disease: Exploring How Genetics and Phenotype Influence Risk. J Mol Biol. 2019;431:1805–17. https://doi.org/10.1016/j.jmb.2019.01.045
7. Bellenguez C, Küçükali F, Jansen IE, Kleineidam L, Moreno-Grau S, Amin N, et al. New insights into the genetic etiology of Alzheimer's disease and related dementias. Nat Genet. 2022;54:412–36. https://doi.org/10.1038/s41588-022-01024-z
8. Rexach JE, Polioudakis D, Yin A, Swarup V, Chang TS, Nguyen T, et al. Tau Pathology Drives Dementia Risk-Associated Gene Networks toward Chronic Inflammatory States and Immunosuppression. Cell Rep. 2020;33:108398. https://doi.org/10.1016/j.celrep.2020.108398
9. Liddelow SA, Guttenplan KA, Clarke LE, Bennett FC, Bohlen CJ, Schirmer L, et al. Neurotoxic reactive astrocytes are induced by activated microglia. Nature. 2017;541:481–7. https://doi.org/10.1038/nature21029
10. Vogels T, Murgoci A-N, Hromádka T. Intersection of pathological tau and microglia at the synapse. Acta Neuropathol Commun. 2019;7:109. https://doi.org/10.1186/s40478-019-0754-y
11. Dejanovic B, Wu T, Tsai M-C, Graykowski D, Gandham VD, Rose CM, et al. Complement C1q-dependent excitatory and inhibitory synapse elimination by astrocytes and microglia in Alzheimer's disease mouse models. Nat Aging. 2022;2:837–50. https://doi.org/10.1038/s43587-022-00281-1
12. Wang C, Yue H, Hu Z, Shen Y, Ma J, Li J, et al. Microglia mediate forgetting via complement-dependent synaptic elimination. Science. 2020;367:688–94. https://doi.org/10.1126/science.aaz2288
13. Hong S, Beja-Glasser VF, Nfonoyim BM, Frouin A, Li S, Ramakrishnan S, et al. Complement and microglia mediate early synapse loss in Alzheimer mouse models. Science. 2016;352:712–6. https://doi.org/10.1126/science.aad8373
14. Elmore MRP, Najafi AR, Koike MA, Dagher NN, Spangenberg EE, Rice RA, et al. Colony-stimulating factor 1 receptor signaling is necessary for microglia viability, unmasking a microglia progenitor cell in the adult brain. Neuron. 2014;82:380–97. https://doi.org/10.1016/j.neuron.2014.02.040
15. Green KN, Crapser JD, Hohsfield LA. To Kill a Microglia: A Case for CSF1R Inhibitors. Trends Immunol. 2020;41:771–84. https://doi.org/10.1016/j.it.2020.07.001
16. Luengo E, Buendia I, Fernández-Mendívil C, Trigo-Alonso P, Negredo P, Michalska P, et al. Pharmacological doses of melatonin impede cognitive decline in tau-related Alzheimer models, once tauopathy is initiated, by restoring the autophagic flux. J Pineal Res.

2019;67:e12578. https://doi.org/10.1111/jpi.12578
17. Asai H, Ikezu S, Tsunoda S, Medalla M, Luebke J, Haydar T, et al. Depletion of microglia and inhibition of exosome synthesis halt tau propagation. Nat Neurosci. 2015;18:1584–93. https://doi.org/10.1038/nn.4132
18. Castro-Sánchez S, Zaldivar-Diez J, Luengo E, López MG, Gil C, Martínez A, et al. Cognitive enhancement, TAU phosphorylation reduction, and neuronal protection by the treatment of an LRRK2 inhibitor in a tauopathy mouse model. Neurobiol Aging. Elsevier Inc.; 2020;96:148–54. https://doi.org/10.1016/j.neurobiolaging.2020.09.006
19. Fernández-Mendívil C, Luengo E, Trigo-Alonso P, García-Magro N, Negredo P, López MG. Protective role of microglial HO-1 blockade in aging: Implication of iron metabolism. Redox Biol. Elsevier B.V.; 2021;38. https://doi.org/10.1016/j.redox.2020.101789
20. Yao D, Li R, Hao J, Huang H, Wang X, Ran L, et al. Melatonin alleviates depression-like behaviors and cognitive dysfunction in mice by regulating the circadian rhythm of AQP4 polarization. Transl Psychiatry. 2023;13:310. https://doi.org/10.1038/s41398-023-02614-z
21. Leger M, Quiedeville A, Bouet V, Haelewyn B, Boulouard M, Schumann-Bard P, et al. Object recognition test in mice. Nat Protoc. 2013;8:2531–7. https://doi.org/10.1038/nprot.2013.155
22. Beckelman BC, Yang W, Kasica NP, Zimmermann HR, Zhou X, Keene CD, et al. Genetic reduction of eEF2 kinase alleviates pathophysiology in Alzheimer's disease model mice. J Clin Invest. 2019;129:820–33. https://doi.org/10.1172/JCI122954
23. Deacon RMJ, Rawlins JNP. T-maze alternation in the rodent. Nat Protoc. 2006;1:7–12. https://doi.org/10.1038/nprot.2006.2
24. Miedel CJ, Patton JM, Miedel AN, Miedel ES, Levenson JM. Assessment of Spontaneous Alternation, Novel Object Recognition and Limb Clasping in Transgenic Mouse Models of Amyloid-β and Tau Neuropathology. J Vis Exp. 2017; https://doi.org/10.3791/55523
25. Liu L, Drouet V, Wu JW, Witter MP, Small SA, Clelland C, et al. Trans-synaptic spread of tau pathology in vivo. PLoS One. 2012;7:e31302. https://doi.org/10.1371/journal.pone.0031302
26. de Calignon A, Polydoro M, Suárez-Calvet M, William C, Adamowicz DH, Kopeikina KJ, et al. Propagation of tau pathology in a model of early Alzheimer's disease. Neuron. 2012;73:685–97. https://doi.org/10.1016/j.neuron.2011.11.033
27. Götz J, Deters N, Doldissen A, Bokhari L, Ke Y, Wiesner A, et al. A decade of tau transgenic animal models and beyond. Brain Pathol. 2007;17:91–103. https://doi.org/10.1111/j.1750-3639.2007.00051.x
28. Asai H, Ikezu S, Tsunoda S, Medalla M, Luebke J, Haydar T, et al. Depletion of microglia and inhibition of exosome synthesis halt tau propagation. Nat Neurosci. 2015;18:1584–93. https://doi.org/10.1038/nn.4132
29. Saxena S, Caroni P. Selective neuronal vulnerability in neurodegenerative diseases: from stressor thresholds to degeneration. Neuron. 2011;71:35–48. https://doi.org/10.1016/j.neuron.2011.06.031
30. Burke SN, Barnes CA. Neural plasticity in the ageing brain. Nat Rev Neurosci. 2006;7:30–40. https://doi.org/10.1038/nrn1809
31. Braak H, Alafuzoff I, Arzberger T, Kretzschmar H, Del Tredici K. Staging of Alzheimer disease-associated neurofibrillary pathology using paraffin sections and immunocytochemistry. Acta Neuropathol. 2006;112:389–404. https://doi.org/10.1007/s00401-006-0127-z
32. Frisoni GB, Altomare D, Thal DR, Ribaldi F, van der Kant R, Ossenkoppele R, et al. The probabilistic model of Alzheimer disease: the amyloid hypothesis revised. Nat Rev

Neurosci. 2022;23:53–66. https://doi.org/10.1038/s41583-021-00533-w
33. Small SA, Schobel SA, Buxton RB, Witter MP, Barnes CA. A pathophysiological framework of hippocampal dysfunction in ageing and disease. Nat Rev Neurosci. 2011;12:585–601. https://doi.org/10.1038/nrn3085
34. Rössler M, Zarski R, Bohl J, Ohm TG. Stage-dependent and sector-specific neuronal loss in hippocampus during Alzheimer's disease. Acta Neuropathol. 2002;103:363–9. https://doi.org/10.1007/s00401-001-0475-7
35. West MJ, Kawas CH, Martin LJ, Troncoso JC. The CA1 region of the human hippocampus is a hot spot in Alzheimer's disease. Ann N Y Acad Sci. 2000;908:255–9. https://doi.org/10.1111/j.1749-6632.2000.tb06652.x
36. Shi Y, Yamada K, Liddelow SA, Smith ST, Zhao L, Luo W, et al. ApoE4 markedly exacerbates tau-mediated neurodegeneration in a mouse model of tauopathy. Nature. 2017;549:523–7. https://doi.org/10.1038/nature24016
37. Luengo E, Trigo-Alonso P, Fernández-Mendívil C, Nuñez Á, Campo M del, Porrero C, et al. Implication of type 4 NADPH oxidase (NOX4) in tauopathy. Redox Biol. 2022;49:102210. https://doi.org/10.1016/j.redox.2021.102210
38. Apicco DJ, Ash PEA, Maziuk B, LeBlang C, Medalla M, Al Abdullatif A, et al. Reducing the RNA binding protein TIA1 protects against tau-mediated neurodegeneration in vivo. Nat Neurosci. 2018;21:72–80. https://doi.org/10.1038/s41593-017-0022-z
39. Maurin H, Chong S-A, Kraev I, Davies H, Kremer A, Seymour CM, et al. Early Structural and Functional Defects in Synapses and Myelinated Axons in Stratum Lacunosum Moleculare in Two Preclinical Models for Tauopathy. PLoS One. 2014;9:e87605. https://doi.org/10.1371/journal.pone.0087605
40. Dagher NN, Najafi AR, Kayala KMN, Elmore MRP, White TE, Medeiros R, et al. Colony-stimulating factor 1 receptor inhibition prevents microglial plaque association and improves cognition in 3xTg-AD mice. J Neuroinflammation. 2015;12:139. https://doi.org/10.1186/s12974-015-0366-9
41. Olmos-Alonso A, Schetters STT, Sri S, Askew K, Mancuso R, Vargas-Caballero M, et al. Pharmacological targeting of CSF1R inhibits microglial proliferation and prevents the progression of Alzheimer's-like pathology. Brain. 2016;139:891–907. https://doi.org/10.1093/brain/awv379
42. Peng Y, Liu J, Tang Y, Liu J, Han T, Han S, et al. High-Fat-Diet-Induced Weight Gain Ameliorates Bone Loss without Exacerbating Aβ2PP Processing and Cognition in Female APP/PS1 Mice. Front Cell Neurosci. 2014;8. https://doi.org/10.3389/fncel.2014.00225
43. Sri S, Pegasiou C-M, Cave CA, Hough K, Wood N, Gomez-Nicola D, et al. Emergence of synaptic and cognitive impairment in a mature-onset APP mouse model of Alzheimer's disease. Acta Neuropathol Commun. 2019;7:25. https://doi.org/10.1186/s40478-019-0670-1
44. Takeuchi H, Iba M, Inoue H, Higuchi M, Takao K, Tsukita K, et al. P301S mutant human tau transgenic mice manifest early symptoms of human tauopathies with dementia and altered sensorimotor gating. PLoS One. 2011;6:e21050. https://doi.org/10.1371/journal.pone.0021050
45. Carroll JC, Rosario ER, Chang L, Stanczyk FZ, Oddo S, LaFerla FM, et al. Progesterone and Estrogen Regulate Alzheimer-Like Neuropathology in Female 3xTg-AD Mice. The Journal of Neuroscience. 2007;27:13357–65. https://doi.org/10.1523/JNEUROSCI.2718-07.2007
46. Khan KM, Balasubramanian N, Gaudencio G, Wang R, Selvakumar GP, Kolling L, et al. Human tau-overexpressing mice recapitulate brainstem involvement and neuropsychiatric features of early Alzheimer's disease. Acta Neuropathol Commun. 2023;11:57. https://doi.org/10.1186/s40478-023-01546-5

47. Peng G-P, Feng Z, He F-P, Chen Z-Q, Liu X-Y, Liu P, et al. Correlation of hippocampal volume and cognitive performances in patients with either mild cognitive impairment or Alzheimer's disease. CNS Neurosci Ther. 2015;21:15–22. https://doi.org/10.1111/cns.12317
48. Werneburg S, Jung J, Kunjamma RB, Ha S-K, Luciano NJ, Willis CM, et al. Targeted Complement Inhibition at Synapses Prevents Microglial Synaptic Engulfment and Synapse Loss in Demyelinating Disease. Immunity. 2020;52:167-182.e7. https://doi.org/10.1016/j.immuni.2019.12.004
49. Presumey J, Bialas AR, Carroll MC. Complement System in Neural Synapse Elimination in Development and Disease. Adv Immunol. 2017;135:53–79. https://doi.org/10.1016/bs.ai.2017.06.004
50. Vasek MJ, Garber C, Dorsey D, Durrant DM, Bollman B, Soung A, et al. A complement-microglial axis drives synapse loss during virus-induced memory impairment. Nature. 2016;534:538–43. https://doi.org/10.1038/nature18283
51. Wu X, Gao Y, Shi C, Tong J, Ma D, Shen J, et al. Complement C1q drives microglia-dependent synaptic loss and cognitive impairments in a mouse model of lipopolysaccharide-induced neuroinflammation. Neuropharmacology. 2023;237:109646. https://doi.org/10.1016/j.neuropharm.2023.109646
52. Wu T, Dejanovic B, Gandham VD, Gogineni A, Edmonds R, Schauer S, et al. Complement C3 Is Activated in Human AD Brain and Is Required for Neurodegeneration in Mouse Models of Amyloidosis and Tauopathy. Cell Rep. 2019;28:2111-2123.e6. https://doi.org/10.1016/j.celrep.2019.07.060
53. Dejanovic B, Huntley MA, De Mazière A, Meilandt WJ, Wu T, Srinivasan K, et al. Changes in the Synaptic Proteome in Tauopathy and Rescue of Tau-Induced Synapse Loss by C1q Antibodies. Neuron. 2018;100:1322-1336.e7. https://doi.org/10.1016/j.neuron.2018.10.014
54. van Olst L, Verhaege D, Franssen M, Kamermans A, Roucourt B, Carmans S, et al. Microglial activation arises after aggregation of phosphorylated-tau in a neuron-specific P301S tauopathy mouse model. Neurobiol Aging. 2020;89:89–98. https://doi.org/10.1016/j.neurobiolaging.2020.01.003
55. Carmona-Abellan M, Martinez-Valbuena I, Marcilla I, DiCaudo C, Gil I, Nuñez J, et al. Microglia is associated with p-Tau aggregates in the olfactory bulb of patients with neurodegenerative diseases. Neurol Sci. 2021;42:1473–82. https://doi.org/10.1007/s10072-020-04686-x
56. Schäfer MK, Schwaeble WJ, Post C, Salvati P, Calabresi M, Sim RB, et al. Complement C1q is dramatically up-regulated in brain microglia in response to transient global cerebral ischemia. J Immunol. 2000;164:5446–52. https://doi.org/10.4049/jimmunol.164.10.5446
57. Le LHD, Eliseeva S, Plunk E, Kara-Pabani K, Li H, Yarovinsky F, et al. The microglial response to inhibition of Colony-stimulating-factor-1 receptor by PLX3397 differs by sex in adult mice. Cell Rep. 2025;44:115176. https://doi.org/10.1016/j.celrep.2024.115176
58. Song S, Song S, Cao C, Lin X, Li K, Sava V, et al. Hippocampal neurogenesis and the brain repair response to brief stereotaxic insertion of a microneedle. Stem Cells Int. 2013; https://doi.org/10.1155/2013/205878
59. Unger MS, Schernthaner P, Marschallinger J, Mrowetz H, Aigner L. Microglia prevent peripheral immune cell invasion and promote an anti-inflammatory environment in the brain of APP-PS1 transgenic mice. J Neuroinflammation. BioMed Central Ltd.; 2018;15. https://doi.org/10.1186/s12974-018-1304-4
60. Jaworski T, Lechat B, Demedts D, Gielis L, Devijver H, Borghgraef P, et al. Dendritic

degeneration, neurovascular defects, and inflammation precede neuronal loss in a mouse model for tau-mediated neurodegeneration. Am J Pathol. 2011;179:2001–15. https://doi.org/10.1016/j.ajpath.2011.06.025
61. Bhaskar K, Konerth M, Kokiko-Cochran ON, Cardona A, Ransohoff RM, Lamb BT. Regulation of tau pathology by the microglial fractalkine receptor. Neuron. 2010;68:19–31. https://doi.org/10.1016/j.neuron.2010.08.023
62. Yoshiyama Y, Higuchi M, Zhang B, Huang S-M, Iwata N, Saido TC, et al. Synapse loss and microglial activation precede tangles in a P301S tauopathy mouse model. Neuron. 2007;53:337–51. https://doi.org/10.1016/j.neuron.2007.01.010
63. Wang C, Fan L, Khawaja RR, Liu B, Zhan L, Kodama L, et al. Microglial NF-κB drives tau spreading and toxicity in a mouse model of tauopathy. Nat Commun. 2022;13:1969. https://doi.org/10.1038/s41467-022-29552-6
64. Zilka N, Stozicka Z, Kovac A, Pilipcinec E, Bugos O, Novak M. Human misfolded truncated tau protein promotes activation of microglia and leukocyte infiltration in the transgenic rat model of tauopathy. J Neuroimmunol. 2009;209:16–25. https://doi.org/10.1016/j.jneuroim.2009.01.013
65. Maphis N, Xu G, Kokiko-Cochran ON, Jiang S, Cardona A, Ransohoff RM, et al. Reactive microglia drive tau pathology and contribute to the spreading of pathological tau in the brain. Brain. 2015;138:1738–55. https://doi.org/10.1093/brain/awv081
66. Li Y, Liu L, Barger SW, Griffin WST. Interleukin-1 mediates pathological effects of microglia on tau phosphorylation and on synaptophysin synthesis in cortical neurons through a p38-MAPK pathway. J Neurosci. 2003;23:1605–11. https://doi.org/10.1523/JNEUROSCI.23-05-01605.2003
67. Kitazawa M, Oddo S, Yamasaki TR, Green KN, LaFerla FM. Lipopolysaccharide-induced inflammation exacerbates tau pathology by a cyclin-dependent kinase 5-mediated pathway in a transgenic model of Alzheimer's disease. J Neurosci. 2005;25:8843–53. https://doi.org/10.1523/JNEUROSCI.2868-05.2005
68. Clayton K, Delpech JC, Herron S, Iwahara N, Ericsson M, Saito T, et al. Plaque associated microglia hyper-secrete extracellular vesicles and accelerate tau propagation in a humanized APP mouse model. Mol Neurodegener. 2021;16:18. https://doi.org/10.1186/s13024-021-00440-9
69. Yoshiyama Y, Higuchi M, Zhang B, Huang SM, Iwata N, Saido TCC, et al. Synapse Loss and Microglial Activation Precede Tangles in a P301S Tauopathy Mouse Model. Neuron. Cell Press; 2007;53:337–51. https://doi.org/10.1016/j.neuron.2007.01.010
70. van Olst L, Verhaege D, Franssen M, Kamermans A, Roucourt B, Carmans S, et al. Microglial activation arises after aggregation of phosphorylated-tau in a neuron-specific P301S tauopathy mouse model. Neurobiol Aging. Elsevier Inc.; 2020;89:89–98. https://doi.org/10.1016/j.neurobiolaging.2020.01.003
71. Brelstaff JH, Mason M, Katsinelos T, Mcewan WA, Ghetti B, Tolkovsky AM, et al. Microglia become hypofunctional and release metalloproteases and tau seeds when phagocytosing live neurons with P301S tau aggregates. Sci. Adv. 2021.
72. Asai H, Ikezu S, Tsunoda S, Medalla M, Luebke J, Haydar T, et al. Depletion of microglia and inhibition of exosome synthesis halt tau propagation. Nat Neurosci. Nature Publishing Group; 2015;18:1584–93. https://doi.org/10.1038/nn.4132
73. Shi Y, Manis M, Long J, Wang K, Sullivan PM, Serrano JR, et al. Microglia drive APOE-dependent neurodegeneration in a tauopathy mouse model. Journal of Experimental Medicine. Rockefeller University Press; 2019;216:2546–61. https://doi.org/10.1084/jem.20190980
74. Dejanovic B, Huntley MA, De Mazière A, Meilandt WJ, Wu T, Srinivasan K, et al.

Changes in the Synaptic Proteome in Tauopathy and Rescue of Tau-Induced Synapse Loss by C1q Antibodies. Neuron. Cell Press; 2018;100:1322-1336.e7. https://doi.org/10.1016/j.neuron.2018.10.014
75. Liddelow SA, Guttenplan KA, Clarke LE, Bennett FC, Bohlen CJ, Schirmer L, et al. Neurotoxic reactive astrocytes are induced by activated microglia. Nature. Nature Publishing Group; 2017;541:481–7. https://doi.org/10.1038/nature21029
76. Le LHD, Eliseeva S, Plunk E, Kara-Pabani K, Li H, Yarovinsky F, et al. The microglial response to inhibition of Colony-stimulating-factor-1 receptor by PLX3397 differs by sex in adult mice. Cell Rep. Elsevier B.V.; 2025;44. https://doi.org/10.1016/j.celrep.2024.115176
77. Coughlan GT, Ourry V, Townsend D, Klinger H, Brown JA, Cuppels M, et al. Sex Differences in P-Tau217, Tau Aggregation, and Cognitive Decline. JAMA Neurol [Internet]. 2026; https://doi.org/10.1001/jamaneurol.2025.5670
78. Coughlan GT, Klinger HM, Boyle R, Betthauser TJ, Binette AP, Christenson L, et al. Sex Differences in Longitudinal Tau-PET in Preclinical Alzheimer Disease: A Meta-Analysis. JAMA Neurol [Internet]. 2025;82:364–75. https://doi.org/10.1001/jamaneurol.2025.0013
79. Wang YT, Therriault J, Servaes S, Tissot C, Rahmouni N, Macedo AC, et al. Sex-specific modulation of amyloid-β on tau phosphorylation underlies faster tangle accumulation in females. Brain. Oxford University Press; 2024;147:1497–510. https://doi.org/10.1093/brain/awad397

DECLARATIONS

- **Consent for publication**

All authors have read and approved the manuscript for publication

- **Availability of data and materials**

Data and materials will be available upon request.

- **Competing interests**

Authors declare no competing interest.

- **Ethics and Consent to Participate**

Not applicable

- **Funding**

This work was supported by the Spanish Ministry of Science, Innovation and Universities PDC2022-133809-I00 and PID2021-125986OB-I00 to MGL, and PID2023-151105OB-I00 to J.A.B; and the General Council for Research and Innovation of the Community of Madrid P2022/BMD-7230 to MGL. PAT, LV and EDS have fellowships from the Spanish Ministry of Science, Innovation and Universities Refs. FPU16/03239, FPU20/03747 and FPU18/00630,

respectively.

- **Authors' contributions**

PTA and EL contributed equally to this work. **PTA** contributed to the conception and design of the study, performed the experiments, analyzed and interpreted the data, and wrote the manuscript. **EL** contributed to the study's conceptual design, supported its development and reviewed the manuscript. **CFM** conducted research experiments and acquired and analyzed data. **LV** contributed to data analysis and reviewed the manuscript. **NGM and PN** contributed to performing experiments. **EDS** assisted with some behavioral experiments**. JAB** provided AAVs.EDS assisted with some behavioural experiments. **MGL** contributed to the design of the study, the writing of the manuscript and provided funding. All authors read and approved the final manuscript.

- **Acknowledgements**

We would like to thank María Dolores Vallejo from the Confocal Unit of the Universidad Autónoma de Madrid, David Muñoz from the Animal Facilities of the Universidad Autónoma de Madrid and Laura Poza-Viejo for editing assistance with the manuscript.

- **Authors' information (optional)**

CFM and EDS are a former employee of Universidad Autónoma de Madrid and does no longer belong to this Institution.

Table 1. Primary antibodies for Western Blot and immunofluorescence analysis

Antibodies	Host	Clonality	Dilution	ID	Source

AT8	Mouse	Monoclonal	1:500	MN1020	Thermofisher
AT180	Mouse	Monoclonal	1:500	MN1040	Thermofisher
β-Actin	Mouse	Monoclonal	1:50000	A5316	Sigma-Aldrich
CD68	Rat	Monoclonal	1:500	MCA1957GA	Bio-rad
C3	Rat	Monoclonal	1:50	HM1045	Hycult
C1q	Rabbit	Monoclonal	1:1000	ab182451	Abcam
GFP	Rabbit	Polyclonal	1:1000	11-476-C100	Exbio
GFAP	Mouse	Monoclonal	1:1000	MAB3402	Sigma-Aldrich
IBA-1	Rabbit	Polyclonal	1:1000	019-19741	Wako
PSD-95	Mouse	Monoclonal	1:1000	MA1-045	Invitrogen
TY9	Rabbit	Polyclonal	1:1000	BML-TA3119-0100	Enzo

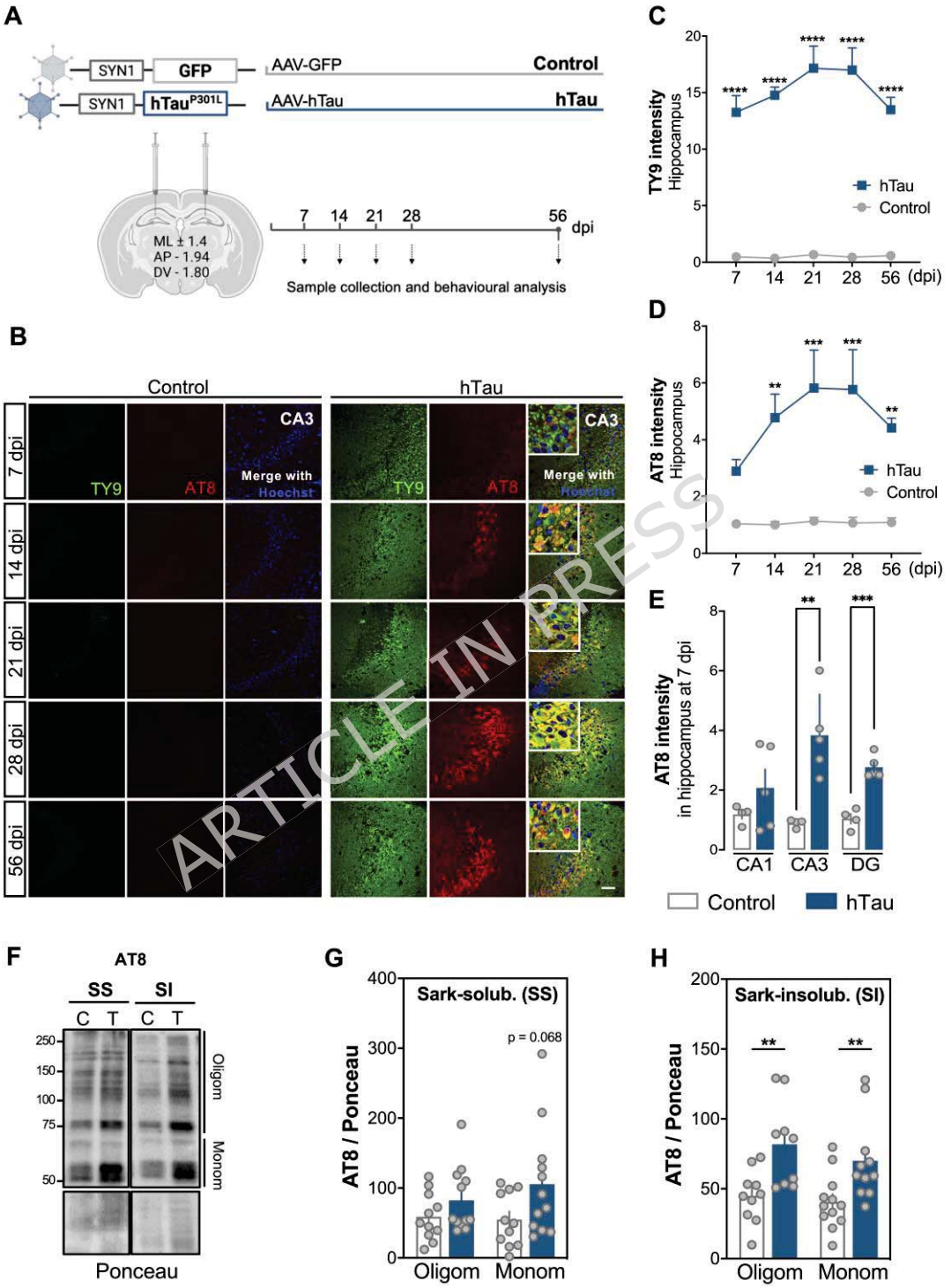

Figure 1

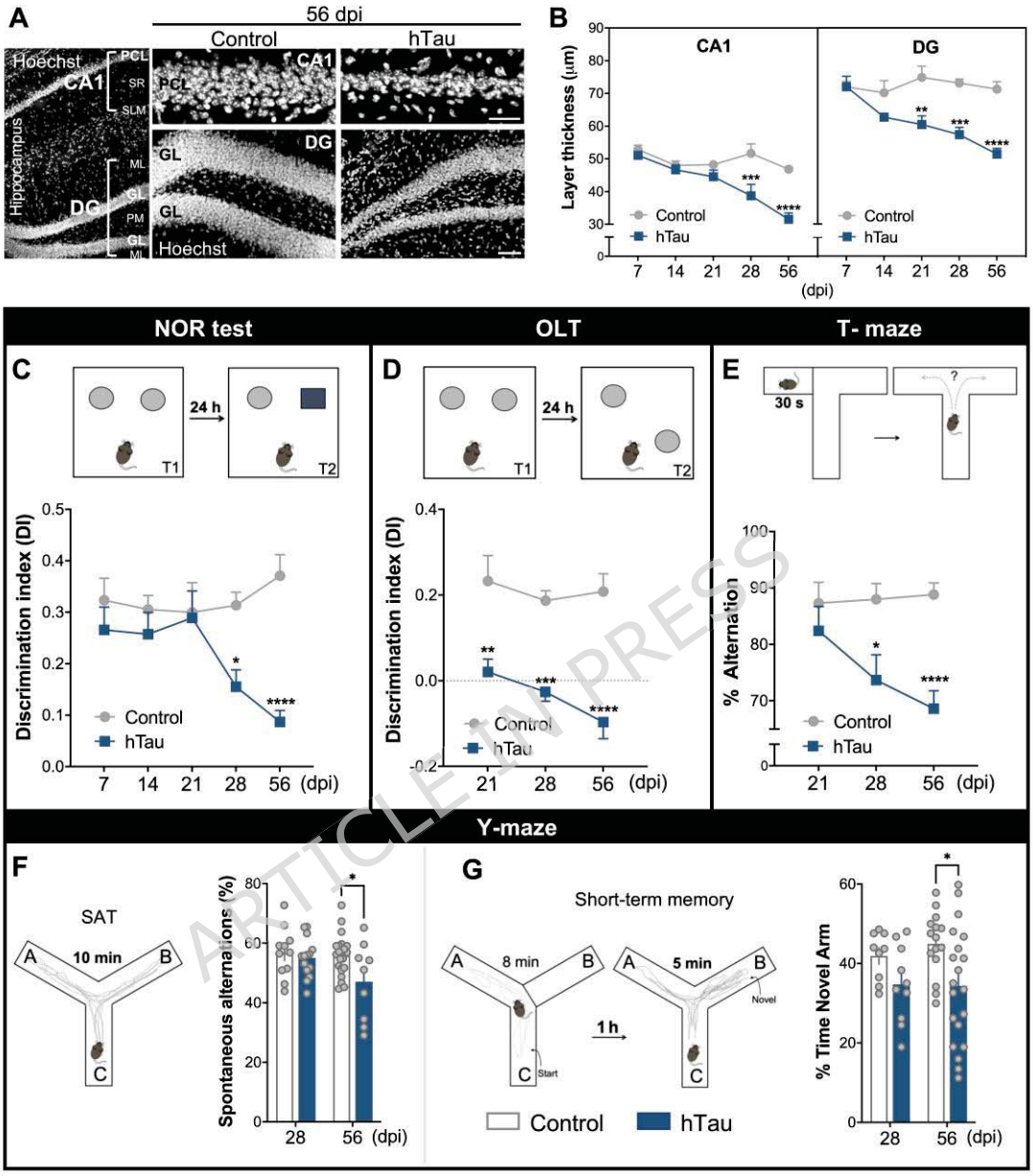

Figure 2

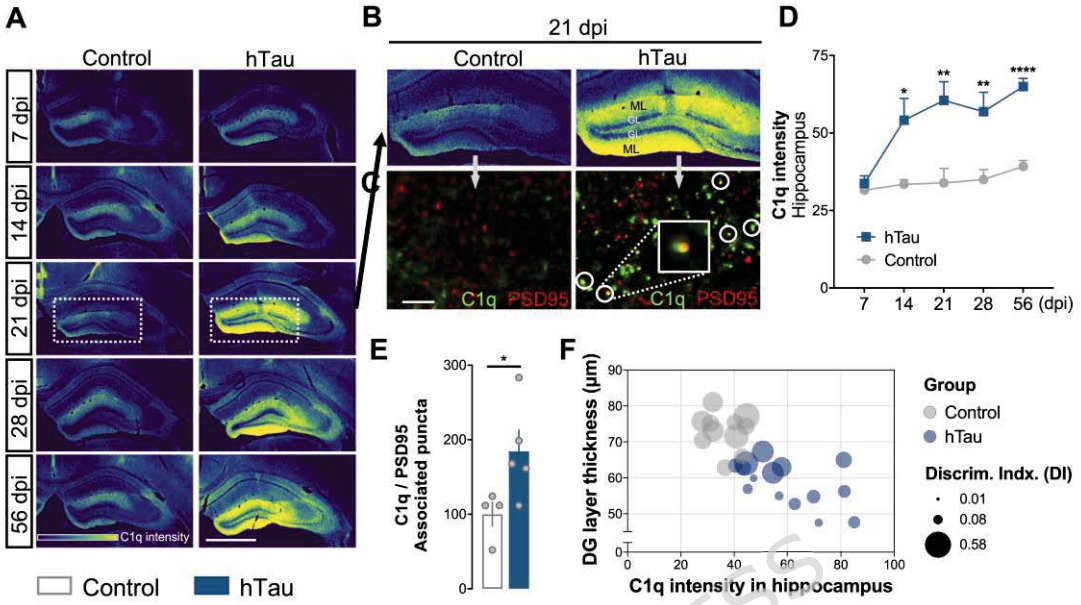

Figure 3

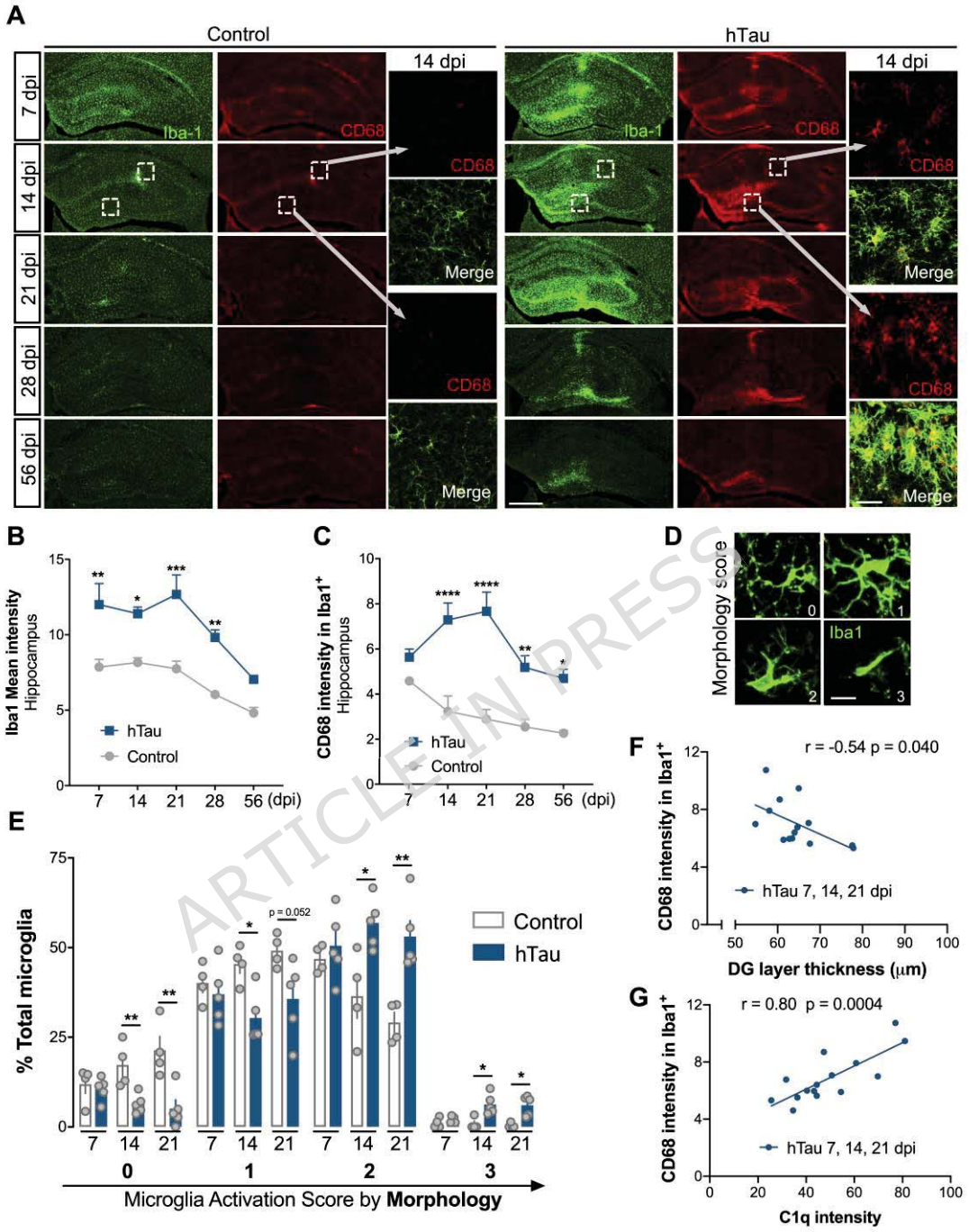
A
Control
hTau
14 dpi
7 dpi
14 dpi
21 dpi
28 dpi
56 dpi
Iba-1
CD68
Merge
B
Iba1 Mean intensity
Hippocampus
hTau
Control
7 14 21 28 56 (dpi)
C
CD68 intensity in Iba1+
Hippocampus
D
Morphology score
Iba1
E
% Total microglia
p = 0.052
Control
hTau
Microglia Activation Score by Morphology
F
r = -0.54 p = 0.040
CD68 intensity in Iba1+
hTau 7, 14, 21 dpi
DG layer thickness (μm)
G
r = 0.80 p = 0.0004
C1q intensity

Figure 4

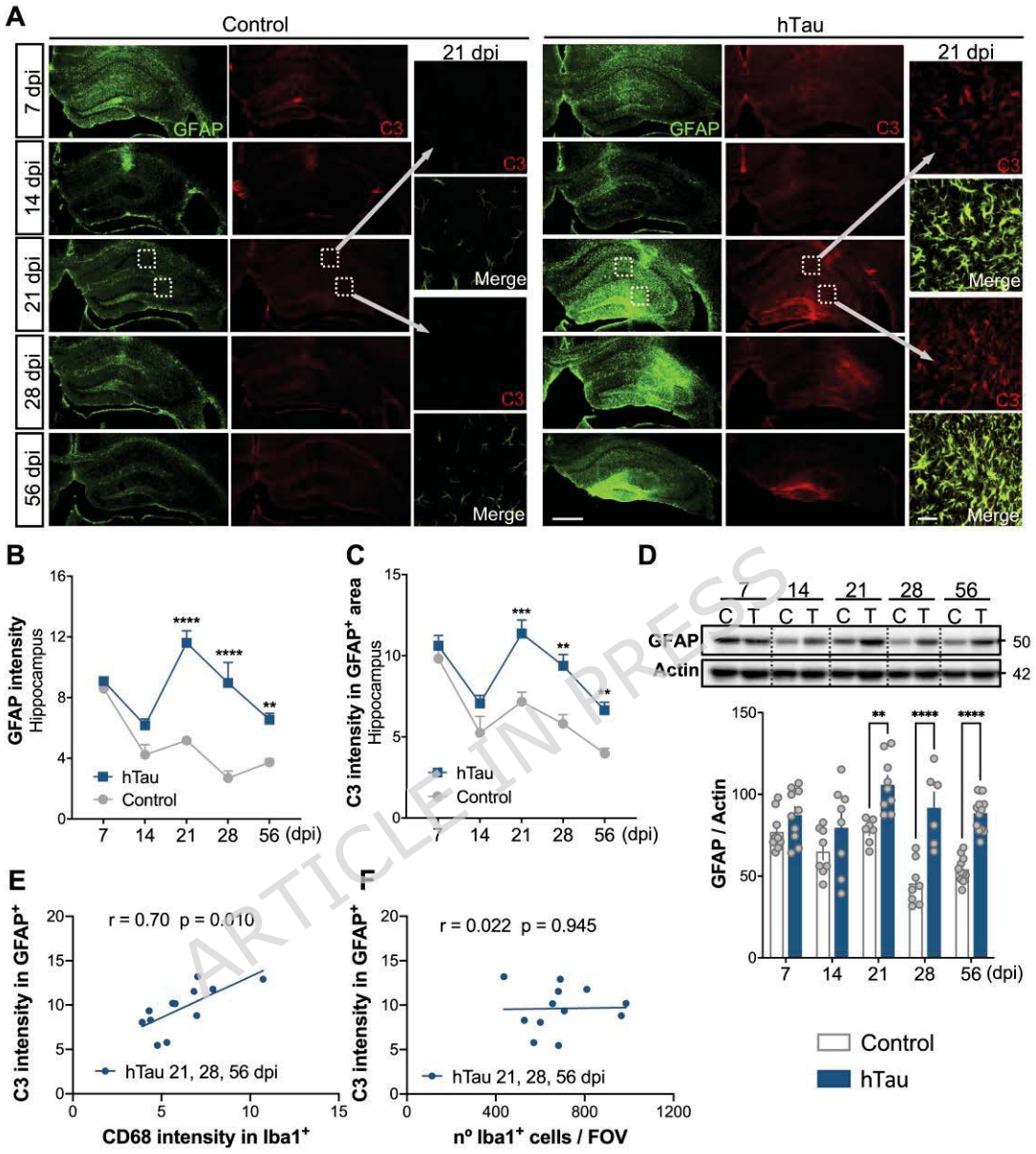

Figure 5

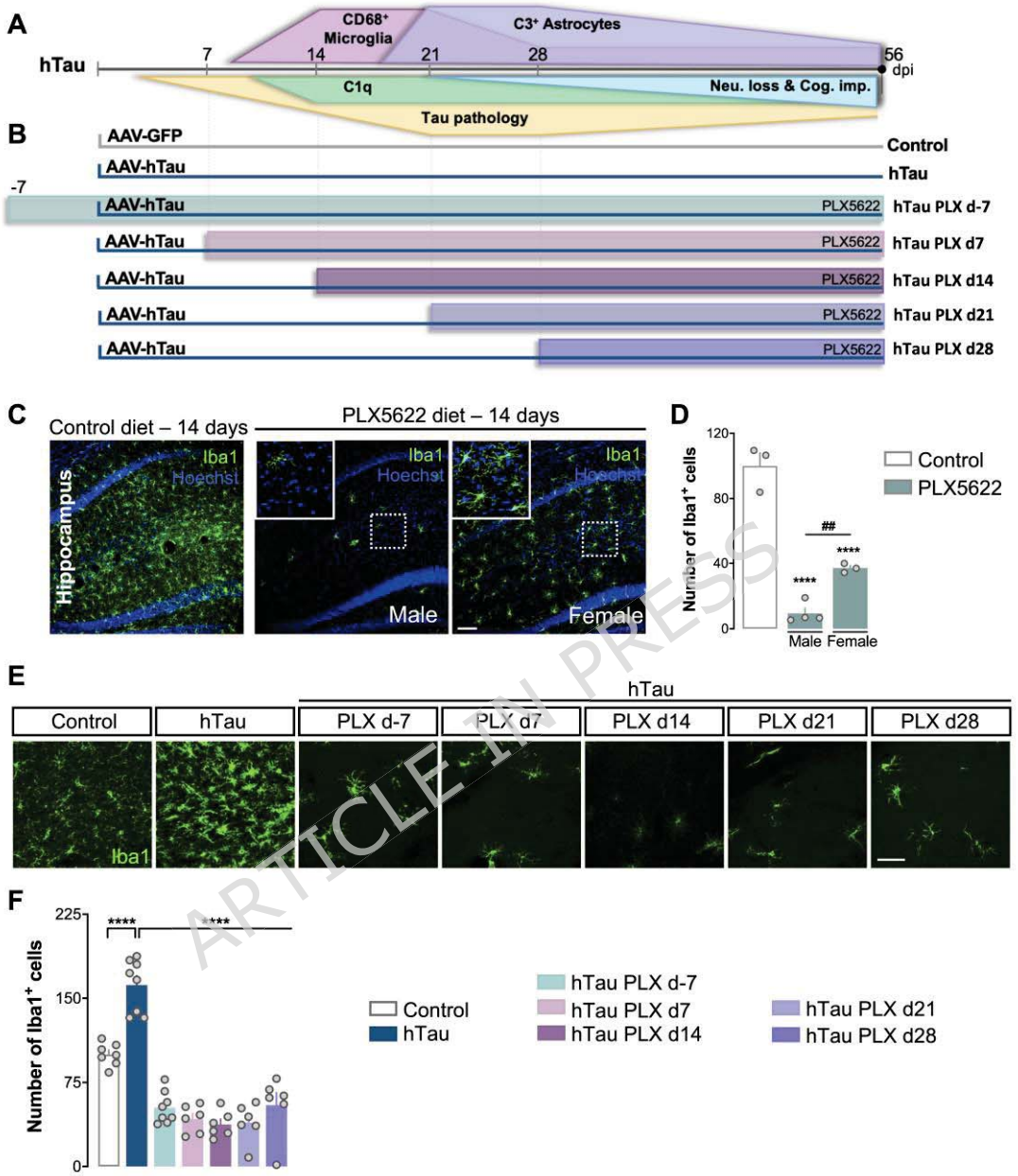

Figure 6

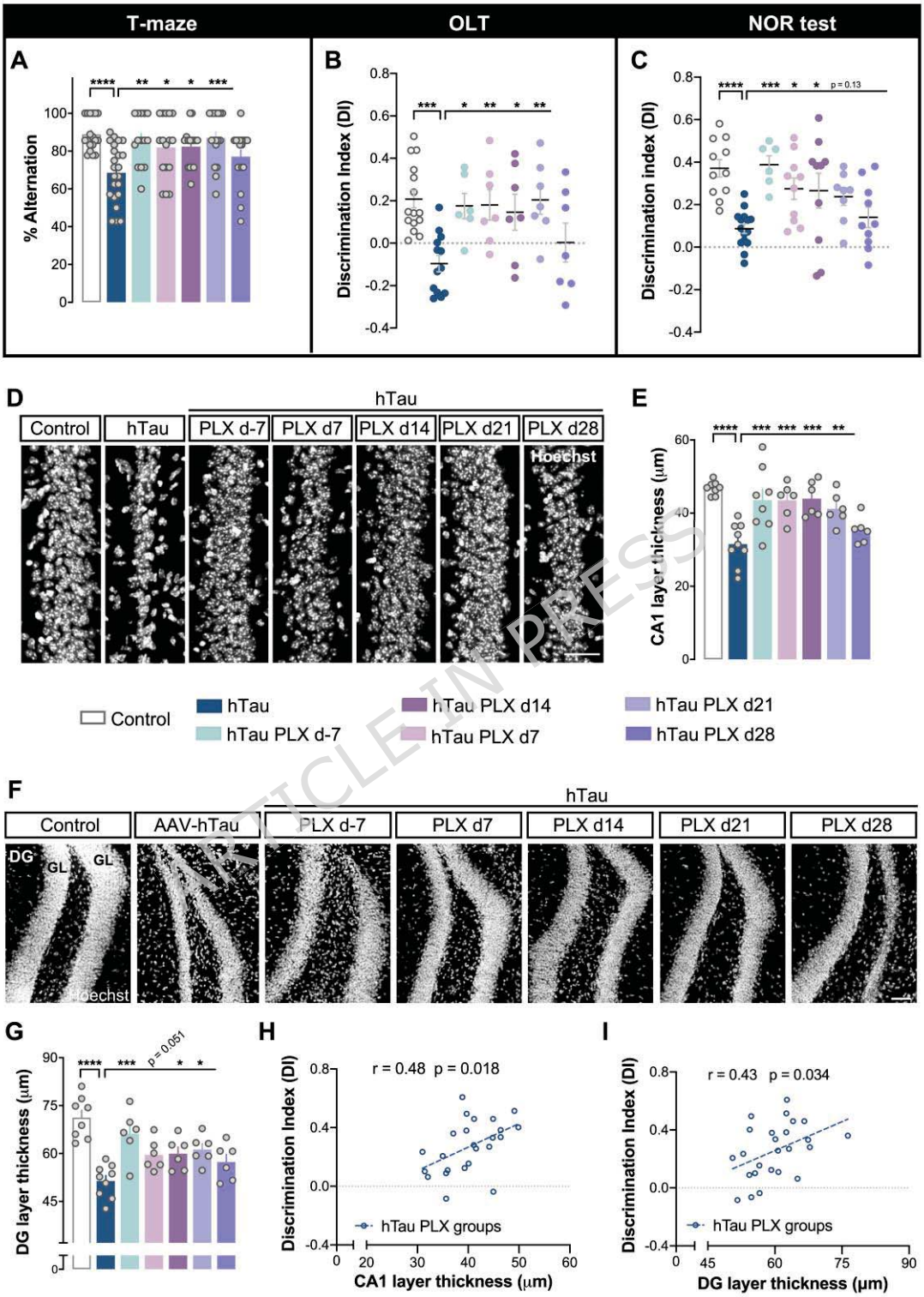
T-maze
OLT
NOR test
A
% Alternation
B
Discrimination Index (DI)
C
Discrimination index (DI)
p = 0.13
D
hTau
Control
hTau
PLX d-7
PLX d7
PLX d14
PLX d21
PLX d28
Hoechst
E
CA1 layer thickness (µm)
Control
hTau
hTau PLX d-7
hTau PLX d14
hTau PLX d7
hTau PLX d21
hTau PLX d28
F
hTau
Control
AAV-hTau
PLX d-7
PLX d7
PLX d14
PLX d21
PLX d28
DG
GL
GL
Hoechst
G
DG layer thickness (µm)
p = 0.051
H
r = 0.48 p = 0.018
Discrimination Index (DI)
hTau PLX groups
CA1 layer thickness (µm)
I
r = 0.43 p = 0.034
Discrimination Index (DI)
hTau PLX groups
DG layer thickness (µm)

Figure 7

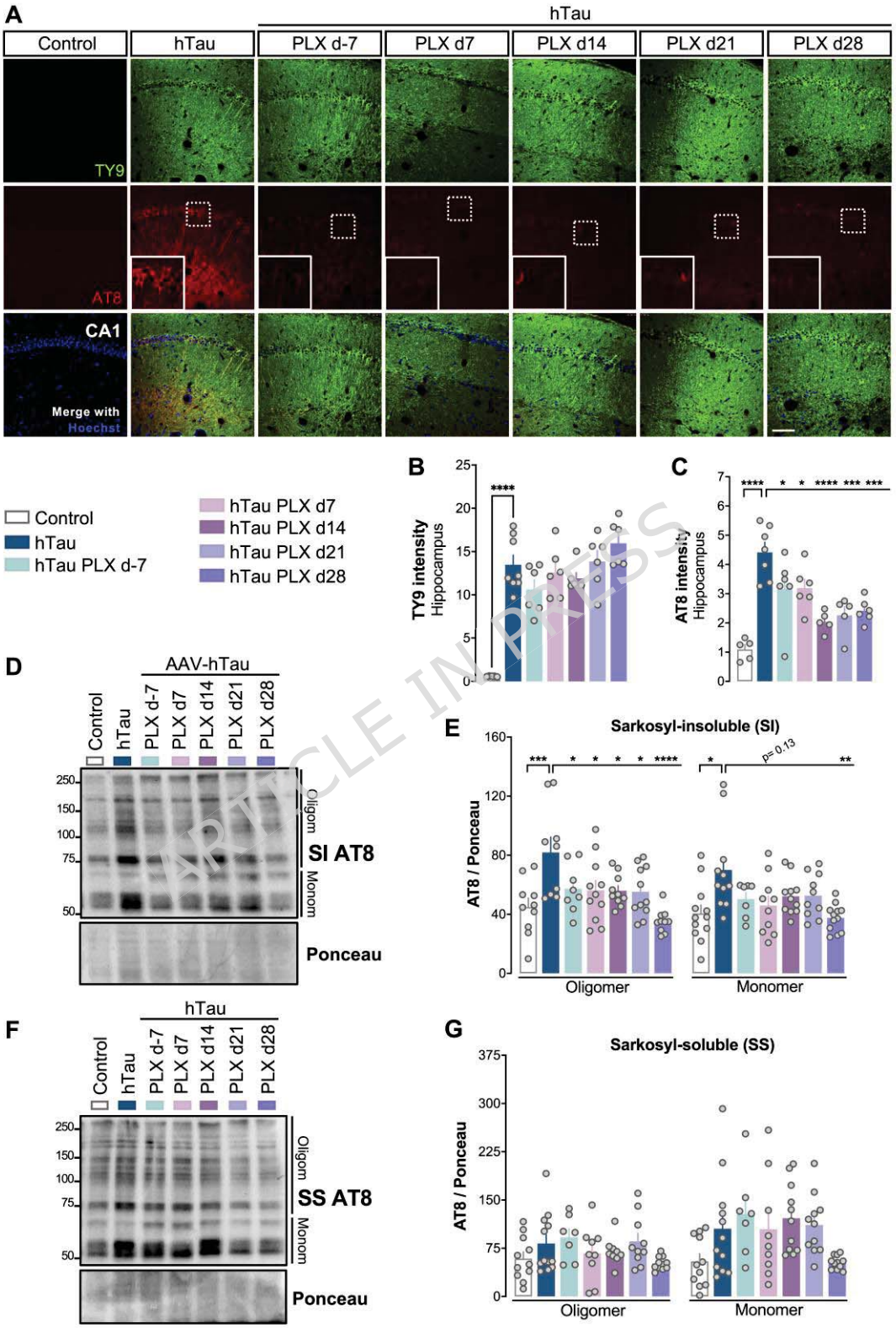
A
hTau
Control
hTau
PLX d-7
PLX d7
PLX d14
PLX d21
PLX d28
TY9
AT8
CA1
Merge with Hoechst
Control
hTau
hTau PLX d-7
hTau PLX d7
hTau PLX d14
hTau PLX d21
hTau PLX d28
B
TY9 intensity Hippocampus
C
AT8 intensity Hippocampus
D
AAV-hTau
Control
hTau
PLX d-7
PLX d7
PLX d14
PLX d21
PLX d28
250
150
100
75
50
Oligom
Monom
SI AT8
Ponceau
E
Sarkosyl-insoluble (SI)
AT8 / Ponceau
Oligomer
Monomer
p= 0.13
F
hTau
SS AT8
Ponceau
G
Sarkosyl-soluble (SS)
AT8 / Ponceau
Oligomer
Monomer

Figure 8

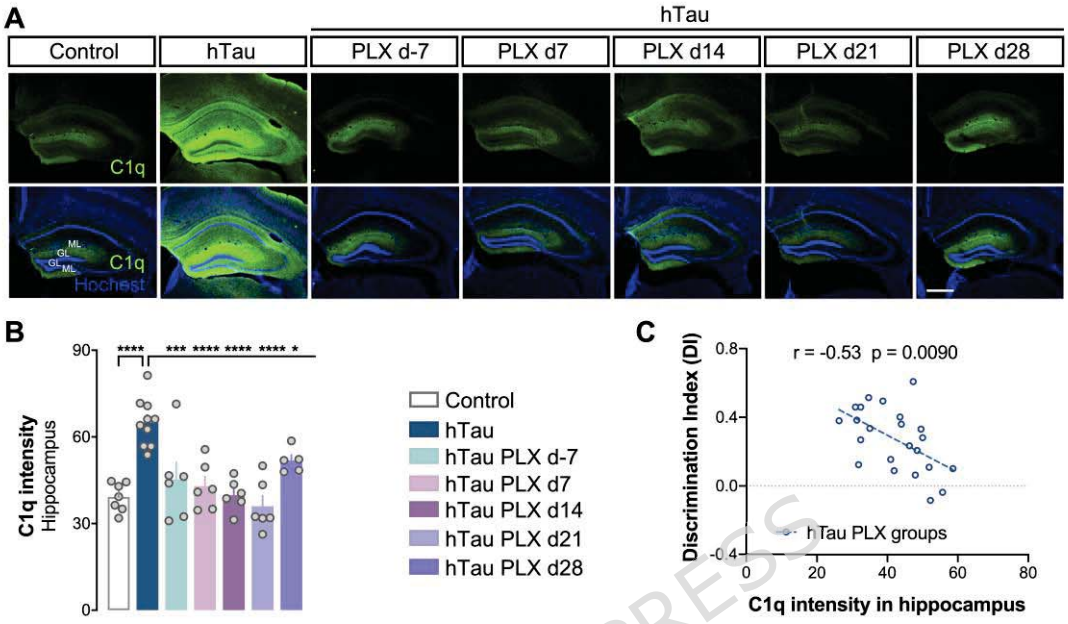

Figure 9

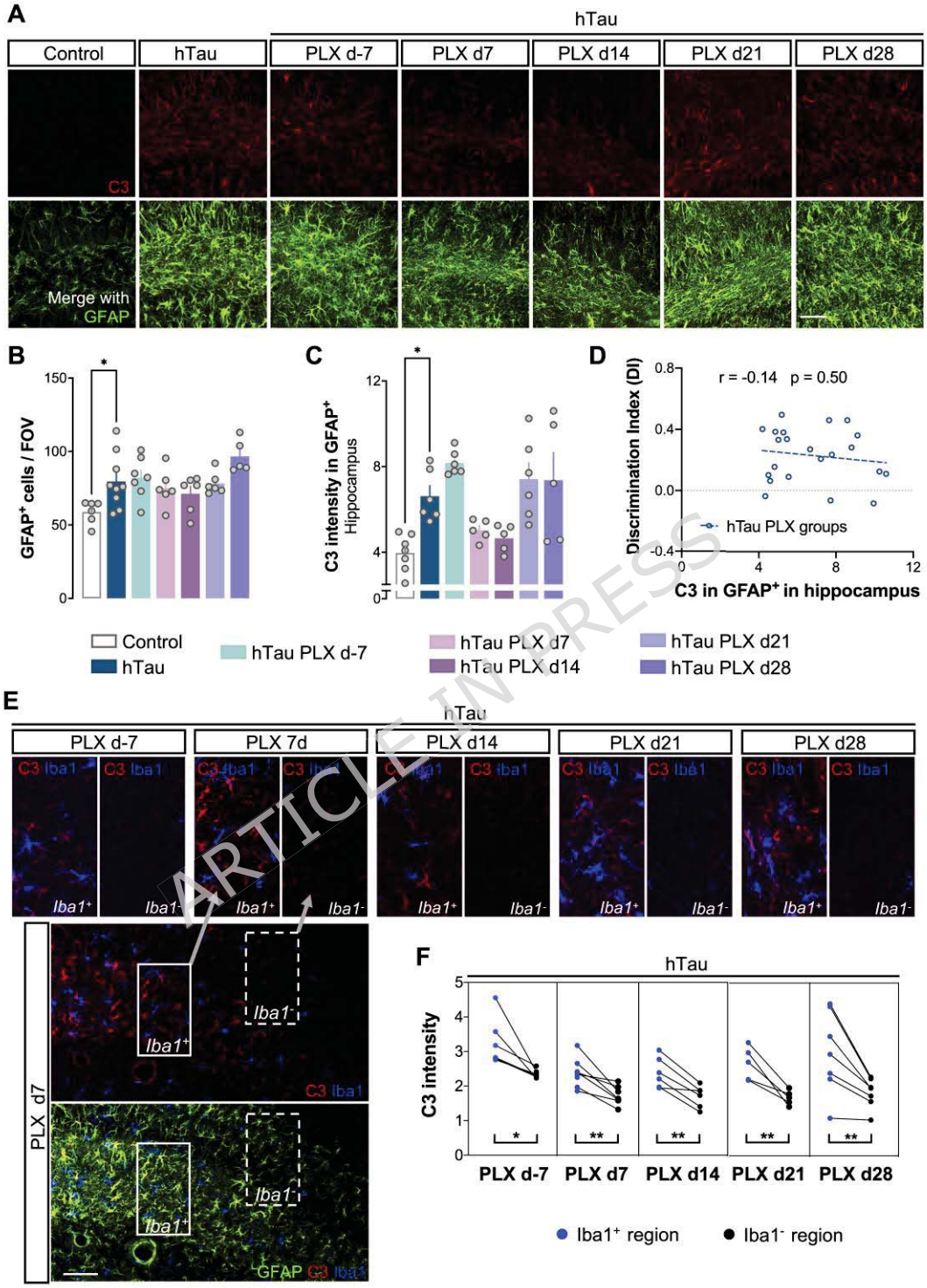
A
hTau
Control
hTau
PLX d-7
PLX d7
PLX d14
PLX d21
PLX d28
C3
Merge with GFAP
B
GFAP+ cells / FOV
C
C3 intensity in GFAP+ Hippocampus
D
Discrimination Index (DI)
r = -0.14 p = 0.50
hTau PLX groups
C3 in GFAP+ in hippocampus
Control
hTau
hTau PLX d-7
hTau PLX d7
hTau PLX d14
hTau PLX d21
hTau PLX d28
E
hTau
PLX d-7
PLX 7d
PLX d14
PLX d21
PLX d28
C3 Iba1
Iba1+
Iba1-
PLX d7
GFAP C3 Iba1
F
hTau
C3 intensity
PLX d-7
PLX d7
PLX d14
PLX d21
PLX d28
Iba1+ region
Iba1- region

Figure 10